Applied Physics A (2026) 132:566
https://doi.org/10.1007/s00339-026-09759-w

Applied Physics A
Materials Science & Processing

Sol-gel synthesis of Ti-Doped ZnO nanoparticles: Contribution of Solvent effects to structural, mechanical, and magnetic properties

Emine Turkmen[1] · Hakan Ada[2] · Elif Asikuzun Tokeser[3] · Serap Safran[4,5] · Özgür Öztürk[6]

Received: 10 April 2026 / Accepted: 22 May 2026
© The Author(s) 2026

Abstract

In this study, $Zn_{1-x}Ti_xO$ ($0 \leq x \leq 0.05$) nanoparticles were synthesized via the sol-gel method, and the effects of monoethanolamine (MEA) and 2-propanol solvents on structural, magnetic, and mechanical properties were comparatively investigated. The originality of the study lies in its systematic and multifaceted analysis of solvent-induced effects. XRD analyses confirmed that the wurtzite structure of ZnO was preserved; however, peak shifts and reductions in crystallite size occurred due to both solvent and doping effects. SEM images revealed that MEA led to more compact and homogeneous structures, while 2-propanol resulted in more porous and irregular morphologies, particularly at lower doping levels. Magnetic measurements showed the development of ferromagnetic behavior. Mechanical tests indicated that samples synthesized with MEA reached a maximum microhardness of 0.556 GPa, whereas 2-propanol-based samples exhibited a fracture toughness as high as 1.89 $MPa.m^{1/2}$. Microhardness data were analyzed using Meyer's law, the PSR, EPD and IIC models, HK approach; RISE behavior was dominant in the MEA system, while ISE behavior prevailed in the undoped and Ti5 samples. These results demonstrate that the ZnO/Ti nanostructures can be optimized for targeted properties through solvent-controlled design, positioning them as strategic material candidates for high-performance applications in sensors, optoelectronic systems, and surface engineering.

Keywords Ti-doped ZnO · Sol-gel · MEA · 2-Propanol · Magnetic Behavior

1 Introduction

Zinc oxide (ZnO) is a semiconductor material that stands out due to its wide band gap (~3.37 eV) and high exciton binding energy (~60 meV). Thanks to its high optical transparency, chemical stability, and ease of synthesis, ZnO is widely used in optoelectronic, piezoelectric, and gas sensor applications. In recent years, extensive research has focused on dilute magnetic semiconductors (DMS) incorporating magnetic dopants into ZnO to enhance its magnetic properties and achieve room-temperature ferromagnetism. DMS materials are promising for spintronic applications due to their ability to simultaneously exhibit electronic and magnetic functionalities. ZnO-based nanoparticles can exhibit ferromagnetic behavior when doped with transition metals such as titanium (Ti), cobalt (Co), iron (Fe), manganese (Mn), and nickel (Ni). In particular, Ti doping not only enhances the magnetic behavior of ZnO but also improves its mechanical, optical, and structural stability properties. The substitution of Zn atoms in the ZnO crystal lattice with Ti atoms alters the spin transport mechanism, 7thereby

✉ Serap Safran
safranserap@gmail.com; safran@science.ankara.edu.tr

[1] Institute of Science, Department of Mechanical Engineering, Kastamonu University, Kastamonu 37150, Turkey

[2] Faculty of Technology, Department of Metallurgical and Materials Engineering, Gazi University, Ankara 06500, Turkey

[3] Faculty of Engineering and Architecture, Department of Metallurgical and Materials Engineering, Kastamonu University, Kastamonu 37150, Turkey

[4] Faculty of Science, Department of Physics, Ankara University, Ankara 06100, Turkey

[5] Ctr Excellence Superconduct Res, 50 Year Campus, Ankara University, Ankara 06830, Turkey

[6] Faculty of Engineering and Architecture, Department of Electrical and Electronics Engineering, Kastamonu University, Kastamonu 37150, Turkey

Published online: 01 June 2026

directly modulating the material's magnetic characteristics [1–7].

Chemical synthesis methods-especially the sol-gel technique-play a key role in the production of ZnO-based DMS nanoparticles. The sol-gel method is preferred for its ability to enable controlled growth and uniform distribution of nanoscale particles at relatively low temperatures. The use of solvents such as monoethanolamine (MEA) and 2-propanol significantly contributes to the improvement of ZnO's crystal structure, surface morphology, and optical properties. The solvent environment determines the particle size and distribution, which in turn can indirectly influence the magnetic performance of the material [8–13].

ZnO nanopowders have attracted significant research interest in recent years due to their low-cost production processes and superior physical properties. A wide body of literature supports that the structural, optical, electrical, and magnetic performance of ZnO can be enhanced through the optimization of production parameters and synthesis methods. Numerous studies have reported that ZnO structures doped with transition metals exhibit ferromagnetic behavior at room temperature [14–23]. However, the origin of ferromagnetism observed in ZnO-based dilute magnetic semiconductors (DMS) remains not fully understood. To clarify this issue, researchers have explored the doping of ZnO with non-magnetic elements. On the other hand, studies focusing specifically on Ti-doped ZnO are relatively limited. Earlier electronic structure calculations suggested the absence of magnetic ordering in Ti-doped ZnO [24]; however, more recent experimental [25] and theoretical investigations [26] have indicated that magnetic ordering may indeed be possible in such systems. Akilan et al. [27] reported defect-induced ferromagnetism in Ti-doped ZnO materials. Similarly, Rajasekaran et al. [10] and Jadhav et al. [28] demonstrated that Ti doping leads to a reduction in crystallite size and an increase in lattice strain. Additionally, the literature notes that the high-temperature mechanical performance of Ti and its alloys has been studied, contributing indirectly to the design of DMS structures [29]. In conclusion, current studies suggest that Ti doping significantly improves the structural, optical, and magnetic properties of ZnO, and that low-temperature synthesis techniques such as the sol-gel method are effective for producing homogeneous and functional DMS nanoparticles.

In this study, Ti-doped ZnO nanoparticles were synthesized using the sol-gel method, and their structural, mechanical, and magnetic properties were thoroughly investigated. One of the novel aspects of this work is the use of two different solvents—monoethanolamine (MEA) and 2-propanol—during the synthesis process. The effects of solvent type and varying Ti concentrations on the crystal structure, surface morphology, magnetic interaction mechanisms, and mechanical strength of the ZnO nanoparticles were systematically analyzed using a range of characterization techniques, including X-ray diffraction (XRD), scanning electron microscopy (SEM), vibrating sample magnetometry (VSM), and microhardness testing. This comprehensive evaluation aims to elucidate the influence of solvent environment and Ti doping level on the properties of ZnO-based dilute magnetic semiconductors, thereby contributing uniquely to the development of advanced materials for applications in spintronics, magnetic storage, and sensor technologies.

2 Materials and methods

2.1 Preparation of Ti (IV)-Doped ZnO samples with MEA additive

In this study, preliminary sol-gel experiments were conducted to determine the optimum processing temperature for the production of Ti-doped and undoped ZnO samples. During this process, $Zn_{1-x}Ti_xO$ (for $x=0.5$) powders were prepared using zinc acetate dihydrate and titanium(IV) butoxide as precursor materials. Methanol and monoethanolamine (MEA) were used as solvents to obtain a homogeneous solution.

The chemicals were weighed in appropriate ratios, placed in a beaker with a sealed lid, and stirred using a magnetic stirrer with heating at 50 °C for 8 h until a completely transparent solution was obtained. The beaker was then uncovered to allow controlled evaporation of the solvent at the same temperature, and the solution was left to gel. The resulting gels were subjected to preliminary thermal treatment and calcined in a muffle furnace at 250 °C for 10 min and 350 °C for 20 min. After calcination, dried residues on the inner walls of the beaker were scraped off using a spatula, and the obtained powders were ground in a mortar to ensure homogeneity.

The powders were divided into two equal portions and subjected to heat treatment at 550 °C and 600 °C for 30 min. Based on XRD analyses, 600 °C was determined to be the optimum annealing temperature. This temperature was later used as the reference annealing condition for the thin film samples to be produced in the subsequent stages of the study.

Following the determination of the optimum temperature, new precursor solutions were prepared with different Ti doping ratios ($0.0<x<0.05$), using methanol and MEA as solvents. These solutions were stirred at 50 °C for 8 h using a magnetic stirrer to ensure homogeneity. Subsequently, the beakers were opened to allow solvent evaporation, and the sol-to-gel transition was completed. The resulting gels were then annealed at the previously determined optimum

temperature of 600 °C for 30 min. After annealing, the powders were pressed into tablets 2 mm in thickness and 10 mm in diameter using a uniaxial press under a pressure of 5 tons for 4 min.

2.2 Preparation of Ti (IV)-Doped ZnO samples with 2-Propanol additive

To evaluate the effect of different solvents in the production of Ti-doped ZnO samples, a second set of experiments was conducted using 2-propanol as the solvent instead of MEA. In this process, $Zn_{1-x}Ti_xO$ ($0.0 < x < 0.05$) samples were again prepared using zinc acetate dihydrate and titanium(IV) butoxide as precursor materials.

The precursors, weighed in appropriate ratios, were mixed with 2-propanol and stirred using a magnetic stirrer at 50 °C for 8 h to obtain a homogeneous solution. Subsequently, the beakers were uncovered and the solutions were evaporated at the same temperature using a magnetic hot plate until gelation was achieved. The resulting gels were subjected to preliminary heat treatment at 250 °C for 10 min and 350 °C for 20 min, followed by calcination in a muffle furnace. After calcination, the powder samples were annealed at 600 °C to perform the thermal treatment at the previously determined optimum temperature.

The obtained powders were ground in a mortar to prevent agglomeration and then pressed into tablets with a thickness of 2 mm and a diameter of 10 mm under a uniaxial pressure of 5 tons for 4 min. These tablets were prepared to comparatively evaluate the effects of different solvents on the mechanical and magnetic properties of ZnO nanoparticles. Sintering of the tablets is a crucial step to strengthen the atomic bonding and reduce crystal defects. For this reason, all tablets prepared using different solvents were subjected to sintering in a muffle furnace at 600 °C for 30 min. As a result of these procedures, Ti-doped ZnO samples were made ready for structural, mechanical, and magnetic characterization analyses.

To ensure the statistical reliability and reproducibility of the mechanical data, microhardness measurements (H_v) were performed by taking the average of at least five independent indentations for each applied load. These indentations were strategically placed on different stabilized regions of the sample surfaces to account for any localized structural variations. The instrumental error margin for the microhardness tester was determined to be within ± 3%, and the reported average values reflect the stable mechanical response of the nanostructures. Similarly, magnetic parameters, including saturation magnetization (M_s) and coercivity (H_c), were extracted from repeated VSM cycles, and the results were found to be consistent within the sensitivity limits of the measurement system. In cases where the calculated standard deviations were smaller than the symbol size in the figures or within the negligible instrumental error range, they were omitted to maintain visual clarity.

3 Results and discussion

3.1 XRD analysis of nanopowder materials

The XRD patterns of undoped and Ti-doped ZnO nanoparticles synthesized via the sol-gel method using two different solvents—MEA and 2-propanol—are presented in Fig. 1. The corresponding crystallite sizes and lattice parameters obtained from these analyses are also listed comparatively in Table 1.

The XRD patterns of undoped and Ti-doped ZnO nanoparticles synthesized using MEA and 2-propanol solvents via the sol-gel method are presented in Fig. 1, while the corresponding crystallite sizes and lattice parameters are comparatively listed in Table 1. In all samples prepared with both solvents, distinct diffraction peaks corresponding to the (100), (002), and (101) planes of the hexagonal wurtzite phase of ZnO were identified. This indicates that the fundamental crystal structure of ZnO was preserved regardless of doping concentration, and no secondary phase formation was observed [30, 31]. However, in the doped samples, slight peak shifts—particularly in the (101) plane—were observed when compared to undoped ZnO. These shifts occurred toward higher 2θ angles, suggesting that the substitution of larger Zn^{2+} ions (0.74 Å) with smaller Ti^{4+} ions (0.60 Å) led to lattice contraction and internal compressive strain. This structural change confirms that Ti^{4+} ions were successfully incorporated into the ZnO lattice in both solvent systems [32]. The incorporation of Ti^{4+} into the Zn^{2+} sites necessitates a charge compensation mechanism due to the valence difference between the ions. This imbalance is likely compensated through the formation of intrinsic defects, predominantly oxygen vacancies (V_O), which maintain the overall charge neutrality of the wurtzite lattice. These structural defects not only influence the lattice parameters but also play a critical role in the subsequent magnetic and mechanical behavior of the nanostructures.

The crystallite size data indicate that Ti doping caused distortions and reductions in the crystalline structure. In the samples synthesized with MEA, the crystallite size ranged from 13.78 to 16.27 nm, showing a notable decrease compared to the undoped ZnO (24.12 nm). This reduction is also supported by the broadening of diffraction peaks in the XRD patterns. MEA likely forms stronger complexes with Zn^{2+} ions, which restricts crystal growth and results in higher internal stress and defect density. In contrast, the crystallite sizes in samples synthesized with 2-propanol were found

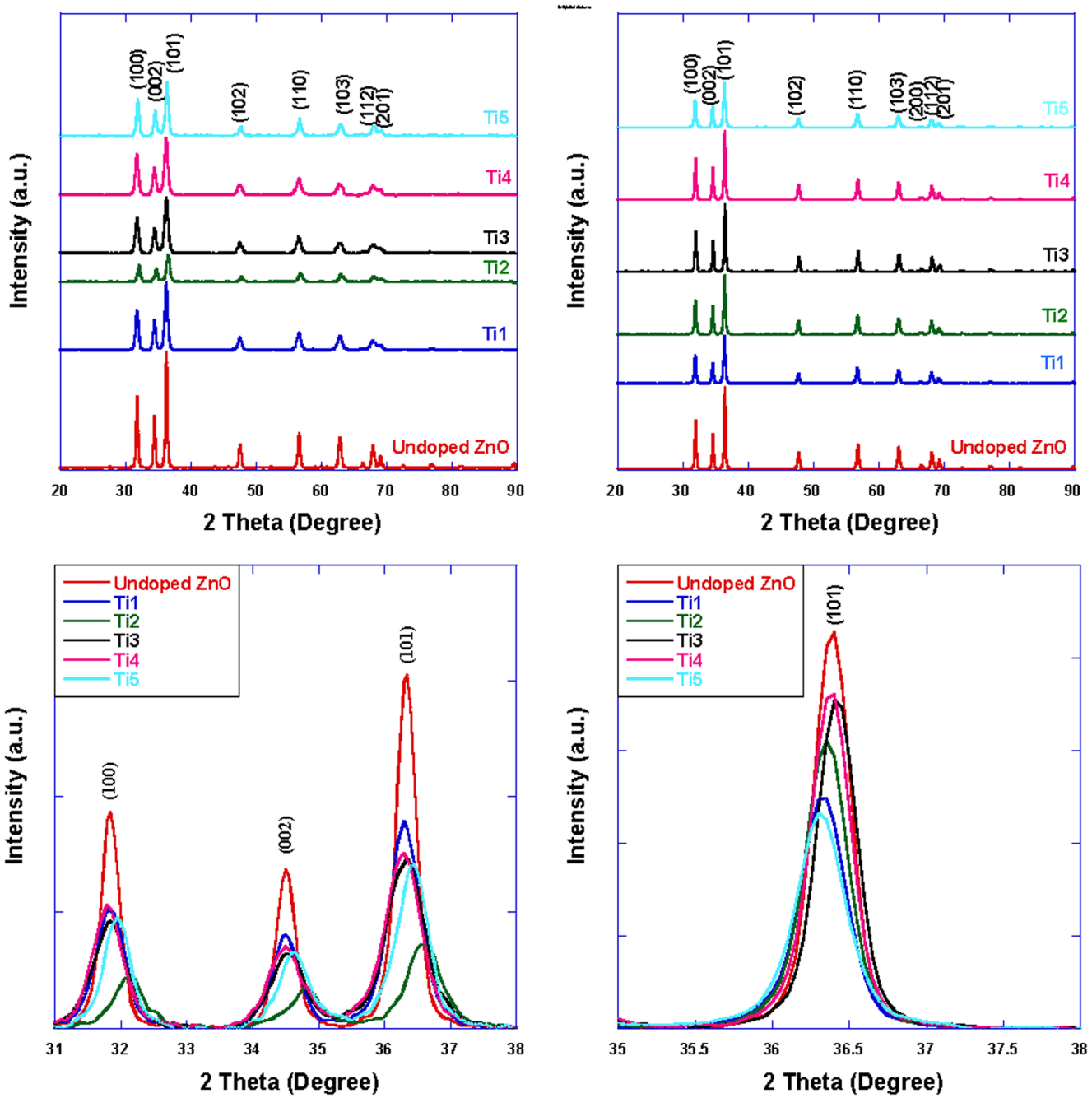


Fig. 1 Comparison of XRD patterns of undoped and Ti doped ZnO nanoparticles synthesized using MEA and 2-Propanol solvents

to be in the range of 20.36–27.88 nm, indicating the formation of larger crystals. The weaker complexation behavior of 2-propanol may have led to more random and irregular crystal growth while allowing the lattice to form under relatively lower internal strain. Nevertheless, increased doping levels in this group also resulted in broader peaks and reduced intensities, indicating a higher density of structural defects.

Nevertheless, increased doping levels in this group also resulted in broader peaks and reduced intensities, indicating a higher density of structural defects. This observed reduction in crystallite size (D) is primarily attributed to the solute drag effect induced by the ionic radius mismatch between Ti^{4+} (0.60 Å) and Zn^{2+} (0.74 Å), which significantly limits grain boundary mobility and "pins" the growth process. In the MEA system, this effect is further intensified by the strong capping and chelating action of the solvent, which increases the nucleation density while providing a thermodynamic barrier to the expansion of individual crystal lattices. Consequently, the combination of lattice strain and solvent-mediated growth inhibition results in the

Table 1 Comparison of crystal size and lattice parameters of ZnO and Ti doped ZnO nanoparticles prepared with MEA and 2-Propanol solvents

Solvent Type	Samples	D (nm)	a (Å)	c (Å)	c/a
MEA	Undoped ZnO	24.12	3.24	5.19	1.60
	Ti1	15.64	3.23	5.19	1.60
	Ti2	16.07	3.21	5.15	1.60
	Ti3	13.78	3.24	5.19	1.60
	Ti4	14.27	3.24	5.19	1.60
	Ti5	16.27	3.23	5.17	1.60
2-Propanol	Undoped ZnO	35.01	3.25	5.20	1.60
	Ti1	24.67	3.24	5.18	1.59
	Ti2	20.36	3.24	5.21	1.60
	Ti3	24.07	3.24	5.20	1.60
	Ti4	22.12	3.24	5.20	1.60
	Ti5	27.88	3.21	5.17	1.61

*All values are reported as the mean of five independent measurements. The experimental error margin for H_v is within 3% based on the calibration standard of the equipment

refined, highly strained nanostructures observed at higher doping concentrations.

When evaluating the lattice parameters, although no significant deviations were observed in the *a* and *c* axes of the samples synthesized using either solvent, slight fluctuations were recorded depending on the doping concentration. A noticeable decrease in the *c* parameter was observed in the MEA-based samples, whereas this parameter remained relatively stable in the samples prepared with 2-propanol. The *c/a* ratio was generally maintained around 1.60; however, slight distortions in structural symmetry were indicated by a ratio of 1.59 in the Ti1 sample and 1.61 in the Ti5 sample synthesized with 2-propanol [33, 34].

The angular shifts observed in the XRD patterns can be primarily attributed to internal lattice strain, the incorporation of Ti ions into the ZnO lattice, reductions in crystallite size, and post-annealing structural rearrangements. In this context, the type of solvent plays a decisive role in the crystal growth kinetics and ion complexation behavior. Due to its stronger complex-forming ability, MEA promotes more controlled and oriented crystal growth, but this also results in more pronounced internal stresses within the crystal lattice. In contrast, 2-propanol, with its weaker complexation tendency, allows for more random and multidirectional crystal growth, which leads to relatively lower internal strain within the lattice.

In conclusion, although the fundamental crystal phase of Ti-doped ZnO nanoparticles synthesized using MEA and 2-propanol was preserved, distinct differences in crystallite size, lattice parameters, and internal strain were observed depending on the solvent type. MEA is characterized by higher lattice strain and smaller crystallite sizes, whereas 2-propanol leads to larger crystallites with lower internal strain. However, deviations in the *c/a* ratio observed in some 2-propanol-based samples point to minor disruptions in crystal symmetry. These findings clearly demonstrate that the choice of solvent is a critical parameter directly influencing the structural properties of Ti-doped ZnO systems.

3.2 Evaluation of SEM images of nanopowder materials

Figure 2 presents the SEM images of undoped and Ti-doped ZnO nanoparticles synthesized using MEA and 2-propanol

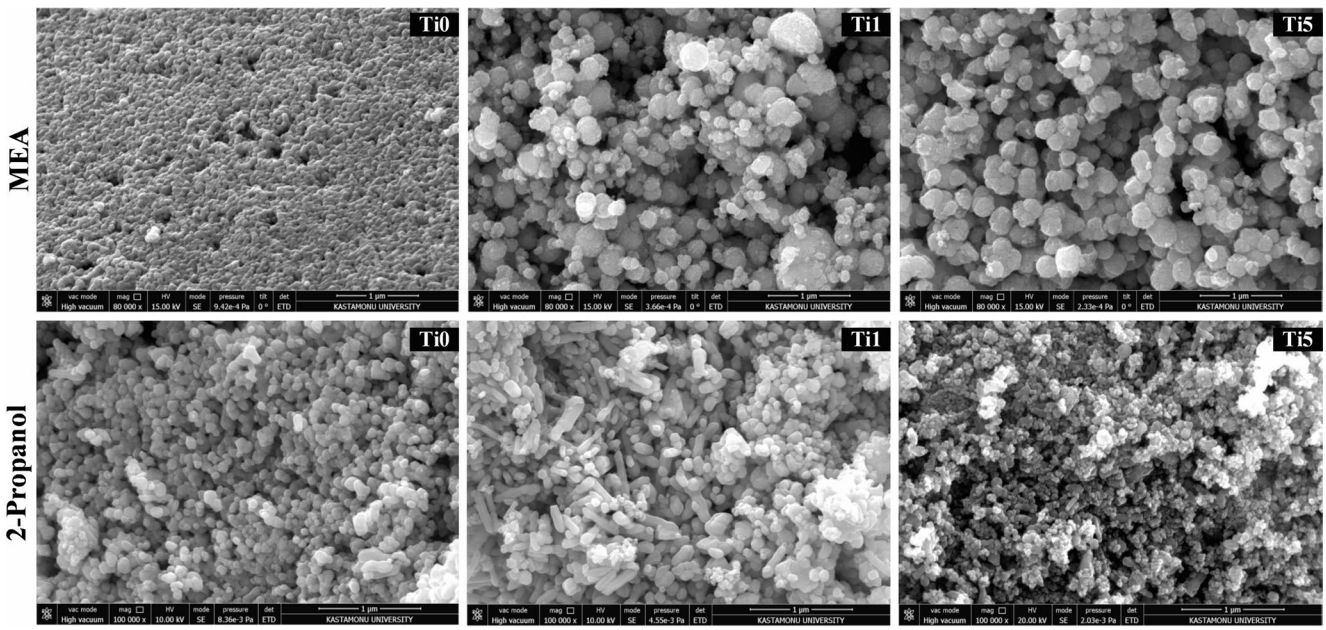


Fig. 2 Comparison of SEM images of undoped and Ti doped ZnO nanoparticles synthesized using MEA and 2-Propanol solvents

as solvents. In the images, Ti0 represents the undoped ZnO sample, while Ti1 and Ti5 correspond to the lowest and highest Ti doping concentrations, respectively. The images clearly demonstrate the effects of both the solvent type and Ti doping level on the surface morphology of the ZnO nanoparticles.

In the samples synthesized using MEA as the solvent, the undoped ZnO (Ti0) exhibited a homogeneous, dense surface morphology with low porosity. With the introduction of Ti doping, spherical nanoparticles began to form, which were particularly evident in the Ti1 and Ti5 samples. As the doping concentration increased (Ti5), the interparticle spacing decreased, resulting in a more tightly packed structure. This indicates that the increased Ti content restricted crystal growth, leading to a more compact and less porous morphology. Additionally, due to MEA's strong complexation ability, the formation of more uniform and spherical particles is observed. The increased particle compactness with higher Ti content may influence the material's mechanical and optical properties, while the slightly porous structures observed at lower doping levels could offer advantages for sensor and catalytic applications.

In the samples prepared with 2-propanol, the undoped ZnO (Ti0) displayed a looser and more porous structure compared to the MEA-based system. Upon Ti doping, crystal formations with rod-like and flower-like morphologies became apparent, especially in the Ti1 and Ti5 samples. These structures suggest that 2-propanol influences the crystallization process in different directions. At higher doping levels (Ti5), smaller and more tightly packed particles were observed, with reduced porosity and a more compact surface morphology. This suggests that above a certain Ti doping threshold, aggregation behavior changes. Furthermore, due to the weaker complexation ability of 2-propanol, crystal growth occurred in more random directions, resulting in a more heterogeneous morphology.

The solvent choice plays a decisive role in directing the crystal habit of the $Zn_{1-x}Ti_xO$ nanostructures. The MEA-assisted synthesis primarily yields spherical-like agglomerates, where the strong chelating nature of the amine and hydroxyl groups ensures uniform growth inhibition across all crystal planes. Conversely, samples prepared with 2-propanol exhibit a distinct transition toward rod-like and complex hierarchical morphologies. This is attributed to the lower capping efficiency of 2-propanol, which allows the lattice strain induced by Ti^{4+} ions to promote anisotropic growth along preferential directions, eventually leading to the rod-and-flower-like evolution observed in the 2-propanol group.

Overall, the SEM images in Fig. 2 reveal that the MEA solvent promotes the formation of more uniform, spherical, and densely packed structures, effectively directing crystal growth. In contrast, the use of 2-propanol led to more complex crystallization behaviors, with rod- and flower-like morphologies, exhibiting looser structures at lower doping levels and a tendency toward compaction at higher concentrations. In both solvents, increasing Ti content reduced interparticle distances and increased compactness, although the mode of morphological development differed depending on the solvent. These findings clearly demonstrate that both solvent type and doping concentration significantly influence the surface morphology of ZnO nanoparticles and thus directly impact their performance in applications such as sensing, photocatalysis, and mechanical coatings.

The morphological transition observed in SEM images is quantitatively supported by the XRD parameters. Specifically, the reduction in crystallite size and the simultaneous increase in lattice strain observed at higher Ti concentrations suggest a high density of nucleation sites and restricted grain growth. This structural refinement leads to a larger surface area, which, in the presence of MEA as a solvent, facilitates the hierarchical assembly of nanoparticles into flower-like clusters rather than simple spherical growth.

3.3 Vickers Microhardness Analysis of Nanopowder Materials

Microhardness is a critical mechanical parameter that reflects the structural and compositional characteristics of solid materials. In recent years, microhardness testing has gained increasing importance in the mechanical characterization of materials [35–39]. Due to its applicability to a wide range of materials and its broad measurement capability, the Vickers microhardness test is one of the most widely used methods. In this study, the microhardness values of undoped and Ti-doped ZnO nanoparticles were determined using a Vickers microhardness testing device.

All samples were subjected to loads of 0.245, 0.490, 0.980, 1.960, and 2.940 N, and corresponding values for microhardness (H_v), elastic modulus (E), yield strength (Y), mean diagonal length (d), and fracture toughness (K_{IC}) were calculated. The results are presented in Table 2. Based on these data, the relationship between applied load and microhardness was plotted in Fig. 3, and the samples were analyzed to determine whether they exhibited Indentation Size Effect (ISE) or Reverse Indentation Size Effect (RISE) behavior. The calculations of H_v, E, Y, and K_{IC} were conducted using the following standard formulas based on the Vickers microhardness testing method.

$$H_v = 1854{,}4 \times \frac{F}{d^2} \tag{1}$$

$$E = 81{,}9635\, H_v \tag{2}$$

Table 2 H_v, E, Y, K_{ic} values calculated depending on the load applied to the specimens

Solvent	Samples	F (*N*)	H_v (GPa)	E (GPa)	Y (GPa)	K_{IC} (MPa/$m^{1/2}$)	H_v (Saturation Region)
MEA	Undoped	0.245	0.412	33.769	0.137	38.01	0.458–0.486
		0.490	0.431	35.326	0.143	38.88	
		0.980	0.458	37.539	0.152	40.08	
		1.960	0.479	39.260	0.159	40.99	
		2.940	0.486	39.834	0.162	41.29	
	Ti1	0.245	0.478	39.178	0.159	30.79	0.508–0.528
		0.490	0.501	41.063	0.167	31.52	
		0.980	0.508	41.637	0.169	31.74	
		1.960	0.526	43.112	0.175	32.30	
		2.940	0.528	43.276	0.176	32.36	
	Ti2	0.245	0.314	25.736	0.104	45.31	0.443–0.461
		0.490	0.386	31.637	0.128	50.24	
		0.980	0.443	36.309	0.147	53.82	
		1.960	0.459	37.621	0.153	54.79	
		2.940	0.461	37.785	0.153	54.91	
	Ti3	0.245	0.307	25.162	0.102	48.16	0.426–0.439
		0.490	0.319	26.146	0.106	49.09	
		0.980	0.426	34.916	0.142	56.73	
		1.960	0.435	35.654	0.145	57.33	
		2.940	0.439	35.981	0.146	57.59	
	Ti4	0.245	0.342	28.031	0.114	48.52	0.434–0.463
		0.490	0.354	29.015	0.118	49.36	
		0.980	0.434	35.572	0.144	54.66	
		1.960	0.462	37.867	0.154	56.39	
		2.940	0.463	37.949	0.154	56.45	
	Ti5	0.245	0.556	45.571	0.185	53.92	0.426–0.480
		0.490	0.526	43.112	0.175	52.44	
		0.980	0.480	39.342	0.16	50.10	
		1.960	0.428	35.080	0.142	47.30	
		2.940	0.426	34.916	0.142	47.19	
2-Propanal	Undoped	0.245	0.515	42.21	0.171	37.88	0.436–0.451
		0.490	0.488	39.99	0.162	36.87	
		0.980	0.451	36.96	0.150	35.45	
		1.960	0.442	36.22	0.147	35.09	
		2.940	0.436	35.73	0.145	34.85	
	Ti1	0.245	0.206	16.88	0.068	56.93	0.305–0.388
		0.490	0.220	18.03	0.073	58.83	
		0.980	0.305	24.99	0.101	69.28	
		1.960	0.385	31.55	0.128	77.83	
		2.940	0.388	31.80	0.129	78.14	
	Ti2	0.245	0.230	18.85	0.076	56.27	0.321–0.419
		0.490	0.276	22.62	0.092	61.64	
		0.980	0.321	26.31	0.107	66.48	
		1.960	0.412	33.76	0.137	75.32	
		2.940	0.419	34.34	0.139	75.95	
	Ti3	0.245	0.245	20.08	0.081	54.14	0.387–0.435
		0.490	0.297	24.34	0.099	59.61	
		0.980	0.387	31.71	0.129	68.05	
		1.960	0.430	35.24	0.143	71.73	
		2.940	0.435	35.65	0.145	72.14	
	Ti4	0.245	0.220	18.03	0.073	54.04	0.364–0.419
		0.490	0.286	23.44	0.095	61.62	
		0.980	0.364	29.83	0.121	69.52	
		1.960	0.423	34.67	0.141	74.94	
		2.940	0.419	34.34	0.139	74.58	
	Ti5	0.245	0.213	17.45	0.071	50.13	0.330–0.388
		0.490	0.269	22.04	0.089	56.34	
		0.980	0.330	27.04	0.110	62.40	
		1.960	0.376	30.81	0.125	66.61	
		2.940	0.388	31.80	0.129	67.67	

$$Y \cong \frac{H_V}{3} \tag{3}$$

$$K_{IC} = \sqrt{2E\alpha} \quad (\alpha, \text{ surface energy}) \tag{4}$$

As shown in Table 2, both E and Y values exhibit a significant dependence on the solvent type and Ti concentration, reflecting the structural integrity of the synthesized nanostructures. Furthermore, the fracture toughness (K_{IC}) was calculated to assess the resistance of the samples to crack propagation. The obtained K_{IC} values (ranging from 1.38 to 2.41 MPa.$m^{1/2}$) are in excellent agreement with the reported literature for ZnO-based ceramics, where values typically fall between 1.0 and 3.0 MPa. $m^{1/2}$. The higher toughness observed in the MEA-based samples is attributed to their more densely packed flower-like morphology, which provides a more tortuous path for crack growth compared to the spherical particles formed in 2-propanol.

Figure 3 illustrates the variation in Vickers microhardness values of undoped and Ti-doped ZnO nanoparticles synthesized using MEA and 2-propanol solvents as a function of applied load (F). The microhardness results reveal that both the type of solvent and the Ti doping concentration have a significant influence on microhardness behavior.

In the samples synthesized with MEA, an increase in microhardness values was observed with increasing load for Ti0 and Ti1-Ti4 samples. This trend indicates the presence of RISE behavior. In contrast, for the Ti5 sample, a decrease in microhardness was observed as the load increased, suggesting that conventional ISE behavior was dominant. In all samples, microhardness values tended to stabilize after approximately 1.5 N, indicating the onset of a plateau region, commonly referred to in the literature as the "saturation region" [40]. Beyond this point, further increases in load had no significant effect on hardness.

In the samples prepared with 2-propanol as the solvent, a noticeable increase in microhardness values was observed with increasing load in Ti-doped specimens, indicating that these samples generally exhibited RISE behavior. In contrast, the undoped ZnO sample showed a decrease in microhardness with increasing load, demonstrating a tendency toward ISE. Additionally, all samples in this group exhibited a stabilization of microhardness values beyond an applied load of approximately 2 N, indicating that the saturation region was reached [39]. This observation suggests that surface effects dominate at low loads, whereas volumetric deformation becomes the determining factor at higher loads.

In the MEA-based samples, lower doping concentrations led to RISE behavior, while higher doping levels (Ti5) resulted in a transition to ISE. In contrast, Ti-doped samples prepared with 2-propanol exhibited an increase in microhardness with increasing doping concentration, and all except the undoped sample demonstrated RISE behavior. For both solvent systems, the change in microhardness ceased beyond a certain load value—approximately 1.5 N for MEA and 2 N for 2-propanol—marking the transition into the saturation region. These differences reveal that the

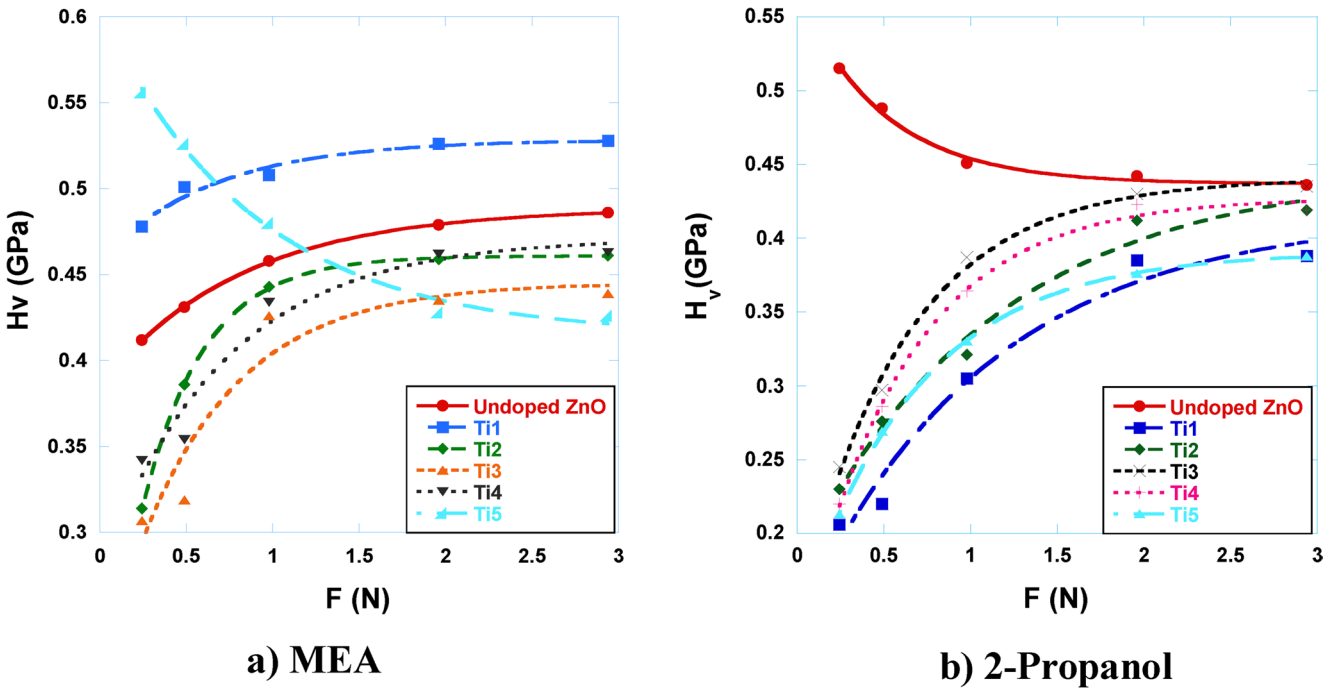


Fig. 3 The variation graph of microhardness values of the samples with respect to the applied load according to the Vickers method

type of solvent and the doping level play a significant role not only in determining the microstructure but also in influencing the mechanical properties of the material. Whether a sample exhibits ISE or RISE behavior provides critical insight into its surface-wave interaction, deformation mechanisms, and potential areas of application.

To further evaluate the microhardness characteristics of materials exhibiting ISE and RISE behavior, various analytical models were employed based on the experimental data. In the literature, several mechanical models have been developed to explain these behaviors [40–43]. In this study, comparative analyses of microhardness were conducted using Meyer's law, the Proportional Sample Resistance (PSR) model, the Elastic/Plastic Deformation (EPD) model, the Hays–Kendall (HK) approach, and the Indentation-Induced Cracking (IIC) model. The calculations and evaluations related to these models are presented in the following section.

3.3.1 Analysis according to Meyer's law

Meyer's law is one of the fundamental models used to describe the relationship between the applied load (F) and the resulting indentation size (d) in microhardness testing. Originally developed by Heinrich Meyer in 1908 [44], this approach is widely employed to evaluate the microhardness behavior of materials under varying load levels. Meyer's law mathematically expresses how the indentation size changes with increasing load applied to the material's surface and defines the relationship between microhardness and load through an empirical coefficient and a constant. This model serves as an important reference point in the mechanical characterization of materials exhibiting either RISE or ISE behavior.

$$F = Ad^n \tag{5}$$

$$lnF = lnA + nln\ d \tag{6}$$

In Meyer's equation, the coefficient n is referred to as the "Meyer's index" or "Meyer's exponent," while A is defined as the material constant. The Meyer exponent (n) is a crucial parameter for describing the deformation characteristics of a material. If $n<2$, the material is considered hard, and there is a non-linear relationship between the applied load and the resulting indentation size. This behavior is typically observed in high-strength and brittle materials. A value of $n=2$ indicates ideal plasticity, suggesting a linear relationship between the load and indentation size, and in this case, the microhardness becomes independent of the applied load. If $n>2$, the material is considered soft, and the microhardness increases with increasing load—behavior that is generally associated with ductile materials. Therefore, the Meyer exponent is regarded as a fundamental criterion for understanding the mechanical response of the tested material [45, 46].

Figure 4 presents the lnF – lnd plots derived from the Meyer model, which describe the relationship between applied load and indentation size for undoped and Ti-doped ZnO nanomaterials. The corresponding values of the Meyer exponent (n) and the logarithmic material constant (lnA) obtained from these graphs are listed in the related tables.

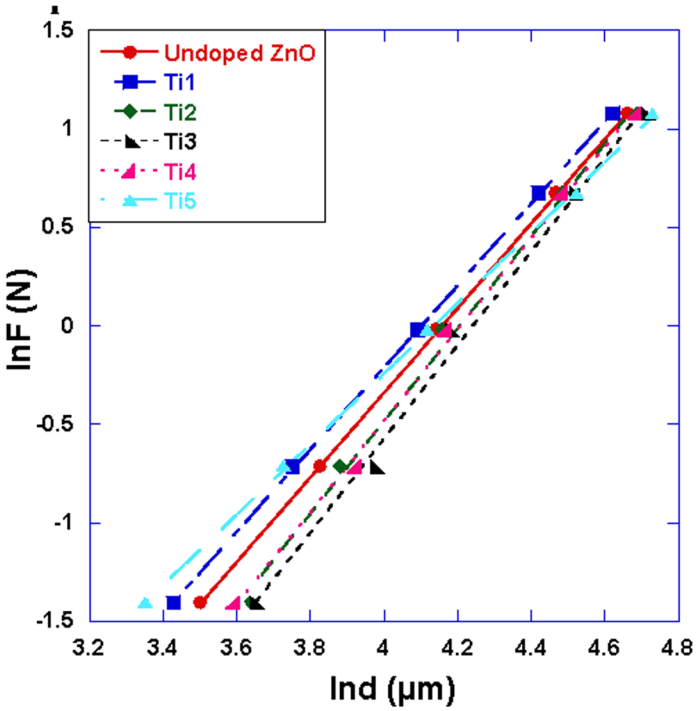
In the samples synthesized with MEA as the solvent, values of $n>2$ were obtained for undoped ZnO and all samples with 1–4% Ti doping. This indicates that these samples exhibit RISE behavior, where microhardness increases with applied load. In contrast, the Ti5 sample showed a value of $n=1.78$, which falls below the threshold of $n=2$, indicating conventional ISE behavior. Additionally, in all MEA-based samples, the fact that $n>1.6$ suggests that these materials exhibit ductile characteristics [43].

In the 2-propanol-based samples, all Ti-doped specimens exhibited $n>2$, confirming RISE behavior, while the undoped ZnO sample showed a value of $n=1.87$, indicating a decrease in microhardness with increasing load and thus ISE behavior. Similarly, all samples in this group had $n>1.6$, confirming that the ZnO structures, whether doped or undoped, possess ductile material characteristics.

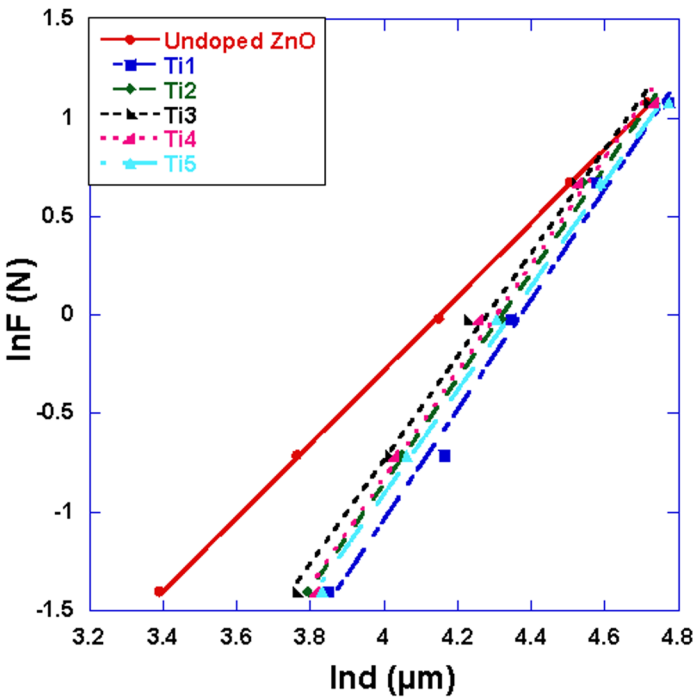
When evaluating the lnF – lnd plots derived from the Meyer model, RISE behavior was predominantly observed in Ti-doped samples with $n>2$. ISE behavior was evident in the Ti5 (MEA) sample and the Ti0 (2-propanol) sample, both of which had $n<2$. All samples exhibited n values greater than 1.6, further confirming their ductile mechanical nature. The 2-propanol solvent showed a more consistent RISE behavior, whereas MEA displayed a transitional behavior depending on the doping level. These findings demonstrate that the Meyer model is an effective method for understanding load-dependent microhardness behavior and for evaluating the ductile or brittle nature of the tested materials.

3.3.2 Analysis according to the proportional sample resistance (PSR) model

The Proportional Sample Resistance (PSR) model is an advanced approach developed to more accurately analyze the relationship between applied load and indentation size in microhardness testing. This model specifically aims to minimize measurement errors that typically arise at low load levels. By assuming that the resistance of the material to indentation is proportional to the applied load, the PSR model addresses the limitations of the conventional



Samples	Meyer Index (n)	InA_K (GPa)
Undoped	2.14	-8.93
Ti1	2.08	-8.53
Ti2	2.34	-9.86
Ti3	2.37	-10.08
Ti4	2.31	-9.75
Ti5	1.78	-7.39



Samples	Meyer Index (n)	InA_K (GPa)
Undoped	1.87	-7.75
Ti1	2.79	-12.20
Ti2	2.67	-11.55
Ti3	2.62	-11.23
Ti4	2.71	-11.69
Ti5	2.63	-11.45

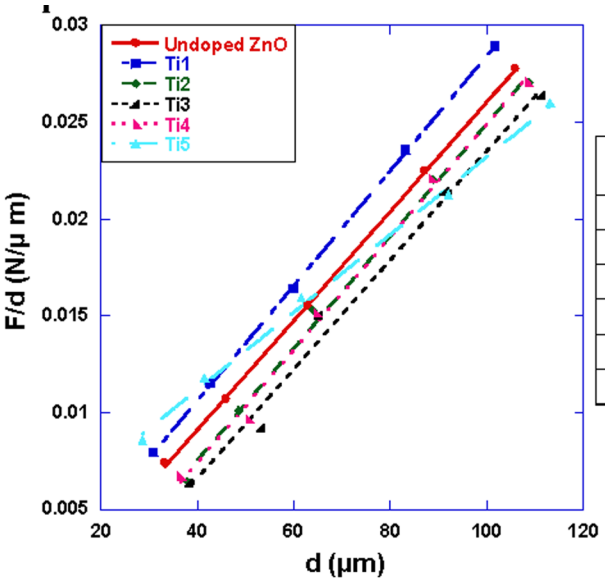
Fig. 4 lnF/lnd graph of samples analyzed according to Meyer's Law

Meyer law. As such, it provides more reliable microhardness calculations at low loads and has become a preferred method in studies that evaluate load-dependent variations in microhardness.

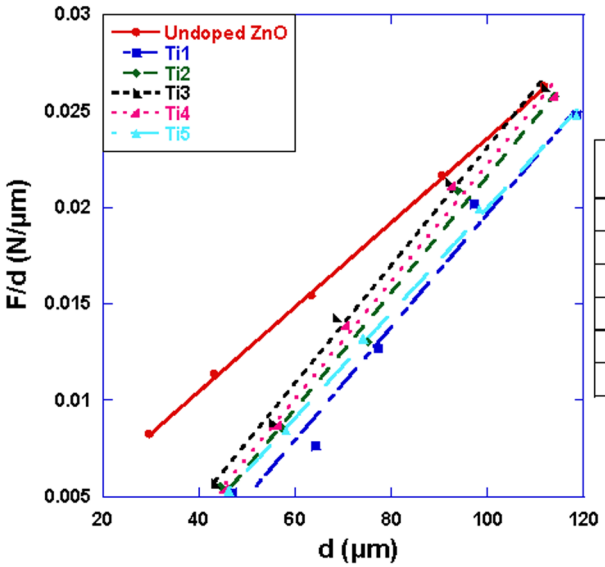
$$\frac{F}{d} = \alpha + \beta\, d \tag{7}$$

$$H_{PSR} = 1854.4\,\beta \tag{8}$$

Figure 5 presents the F/d–d plots generated according to the PSR model for undoped and Ti-doped ZnO samples synthesized using MEA and 2-propanol solvents. Alongside these graphs, the parameters α and β, as well as the load-independent microhardness values (H_{PRS}) were calculated. These



Samples	⊠× 10^{-3} (N)	β× 10^{-4} (N/μm)	H_{PSR} (GPa)	H_V (GPa)
Undoped	-2.1	2.82	0.523	0.458-0.486
Ti1	-1.2	2.96	0.550	0.508-0.528
Ti2	-3.9	2.89	0.536	0.443-0.461
Ti3	-4.6	2.81	0.522	0.426-0.439
Ti4	-4.2	2.91	0.540	0.434-0.463
Ti5	3.1	2.00	0.371	0.426-0.480



Samples	⊠× 10^{-3} (N)	β× 10^{-4} (N/⊠m)	H⊠⊠ (GPa)	H_v (GPa)
Undoped	1.7	2.18	0.404	0.436-0.451
Ti1	-9.6	2.93	0.543	0.305-0.388
Ti2	-8.4	3.01	0.558	0.321-0.419
Ti3	-7.3	3.05	0.565	0.387-0.435
Ti4	-8.1	3.04	0.563	0.364-0.419
Ti5	-7.2	2.72	0.504	0.330-0.388

Fig. 5 F/d - d graph of samples analyzed according to PSR model

graphs allow for the evaluation of the materials' deformation behavior under load based on the mechanical principles underlying the PSR model.

Within the PSR framework, the parameter α serves as an important criterion for assessing the material's load–microhardness relationship. A negative α value indicates RISE behavior, whereas a positive α value corresponds to conventional ISE. Thus, the PSR model provides not only quantitative microhardness values but also meaningful insights into how the material responds to mechanical loading.

In the F/d – d plots for MEA-based samples shown in Fig. 5, the α parameter was found to be negative for the Ti0 and Ti1-Ti4 samples. This indicates that these samples exhibit RISE behavior and that their deformation is predominantly plastic in nature. In contrast, the Ti5 sample exhibited a positive α value (+3.1 × 10^{-3} N), indicating conventional ISE behavior, where both elastic and plastic components contribute to the deformation. These results are consistent with the earlier ISE/RISE assessments made using the Meyer model. However, considering that the H_{PRS} values deviate from the microhardness values observed in the plateau region—where microhardness becomes independent of the applied load—it is evident that the PSR model may have limitations in accurately reflecting the true microhardness of the material [39].

For the samples prepared with 2-propanol, all Ti-doped specimens except the undoped ZnO exhibited negative α values, suggesting RISE behavior and primarily plastic deformation. The undoped ZnO sample showed a positive α value, indicating

ISE behavior. The load-independent microhardness values (H_{PSR}) calculated via the PSR model were significantly lower than the Vickers microhardness values corresponding to the plateau region (above ~1.5–2 N), as observed in the MEA-based system. This further suggests that the PSR model lacks sufficient accuracy in determining absolute microhardness values.

Overall, based on the PSR model, the Ti5 sample in the MEA system displayed ISE behavior, while all others showed RISE behavior. In the 2-propanol system, all doped samples exhibited RISE behavior, except the undoped ZnO, which showed ISE. RISE behavior typically indicates predominant plastic deformation, whereas ISE behavior implies a combination of elastic and plastic deformation. The H_{PSR} values were found to be inadequate in determining absolute, load-independent microhardness and showed notable discrepancies from the plateau region. These findings are generally in agreement with the load–microhardness relationships and deformation mechanisms reported in the literature [36].

3.3.3 Analysis According to the Elastic/Plastic Deformation (EPD) Model

In indentation testing, the size of the impression is typically measured after the indenter has been removed from the material surface. However, due to elastic recovery around the indentation area during this stage, a slight reduction in impression size often occurs. To minimize the error caused by this effect, it has been suggested that a correction term be added to the measured indentation size [38, 47–49]. Based on this approach, the relationship between the applied load and indentation size in the EPD model is defined by Eq. 9, while the load-independent microhardness value is calculated using Eq. 10 [48, 49].

$$F = A_2 + (d_p + d_e)^2 \tag{9}$$

$$H_{EPD} = 1854{,}4 \times A_2 \tag{10}$$

Here, A_2 is a material-specific constant, where d_p represents the plastic deformation coefficient and d_e denotes the elastic deformation coefficient. The values of A_2 and d_e were obtained from the $F^{1/2}$–d_e plot shown in Fig. 6; these values were calculated based on the slope of the graph and its intercept on the y-axis. The corresponding results are presented in the table within the figure. According to the EPD model, the sign of d_e (positive or negative) provides insight into whether elastic or plastic deformation has occurred in the material. A negative d_e value indicates that only plastic deformation took place under the applied load, while a positive d_e suggests that both elastic and plastic deformation occurred.

Figure 6 presents the $F^{1/2}$–d_e plots for Ti-doped ZnO nanoparticles synthesized using MEA and 2-propanol solvents, along with the elastic deformation coefficient (d_e), load-independent hardness (H_{EPD}) and true microhardness (H_v) values obtained from these graphs. When the EPD model was applied to the MEA-based samples, it was observed that the d_e values were negative for all samples except the one with Ti5 doping. This indicates that, for the undoped and Ti1-Ti4 doped samples, deformation under applied load was purely plastic in nature. In contrast, the positive d_e value in the Ti5 sample indicates that both elastic and plastic deformation occurred. These results confirm that RISE behavior is dominant at low doping levels, while ISE behavior becomes prominent at 5% doping.

In the case of 2-propanol-based samples, d_e values were negative for all Ti-doped samples, with the exception of the undoped ZnO sample, which exhibited a positive d_e, suggesting the presence of elastic deformation. This implies that deformation in all Ti-doped samples was entirely plastic. These findings highlight that the solvent type has a pronounced effect on the underlying deformation mechanisms.

Furthermore, when the load-independent microhardness values calculated via the EPD model were compared with the experimentally determined true microhardness values, it was found that the model could not accurately represent the actual microhardness. The fact that the predicted hardness values significantly deviated from those in the plateau region suggests that the EPD model has limited capability in determining absolute microhardness in nanostructured ceramic systems.

3.3.4 Analysis according to the Hays-Kendall (HK) model

Hays and Kendall (1973) proposed that in microhardness measurements, the contact between the indenter and the material does not result in a fully plastic deformation; rather, a portion of the deformation is recovered elastically. According to this approach, part of the applied total load is consumed by elastic recovery, while the remaining portion leads to permanent plastic deformation. Accordingly, they stated that in order for a permanent deformation to occur in the sample, a certain threshold load value (W) must be exceeded. This threshold load represents the elastic limit of deformation and is of critical importance for the accurate calculation of the true microhardness value [50].

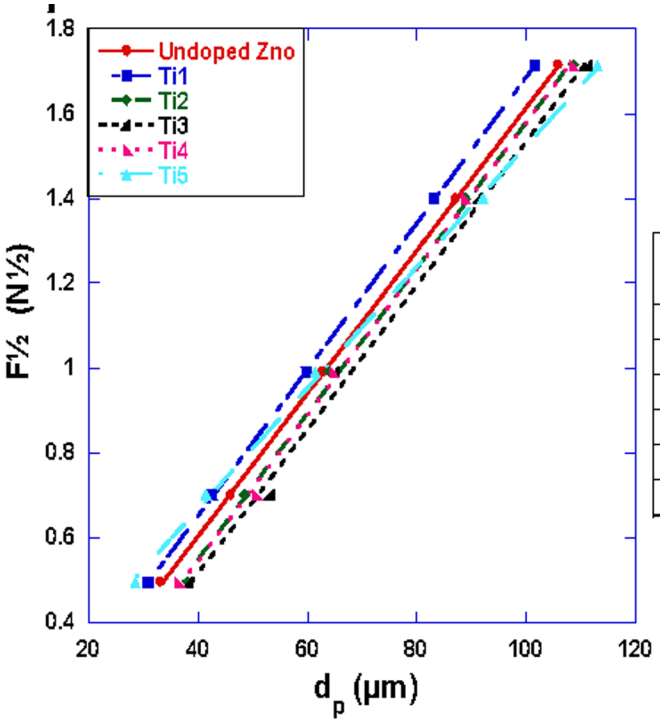
$$F = W_{HK} + A_{HK} d^2 \tag{11}$$

$$H_{HK} = 1854{,}4 \times A_{HK} \tag{12}$$

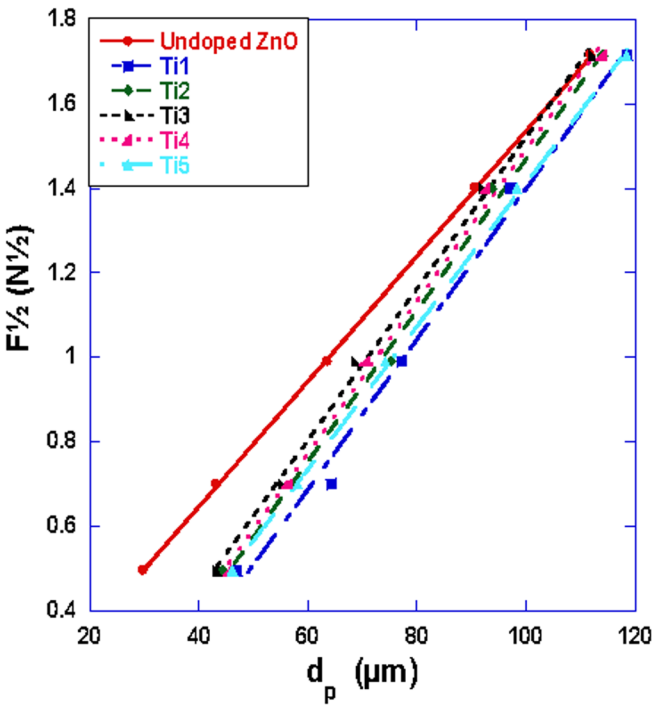
According to the Hays–Kendall (HK) model, the relationship between the applied load and the deformation size is defined by the equation given above (Eq. 11).

Here, W_{HK} represents the minimum load required to produce a permanent indentation in the material, while A_{HK} denotes the load-independent microhardness constant. The HK microhardness value (H_{HK}) is calculated using the expression provided in Eq. 12. The values of W_{HK} and A_{HK} were obtained from the F/d² plots shown in Fig. 7. In these graphs, the slope corresponds to the A_{HK} constant, while the intercept on the y-axis represents W_{HK}, i.e., the minimum pressure required to create an indentation on the sample.

In Fig. 7, the values of W_{HK}, A_{HK} and H_{HK} obtained from the F–d² plots of Ti-doped ZnO samples prepared with MEA

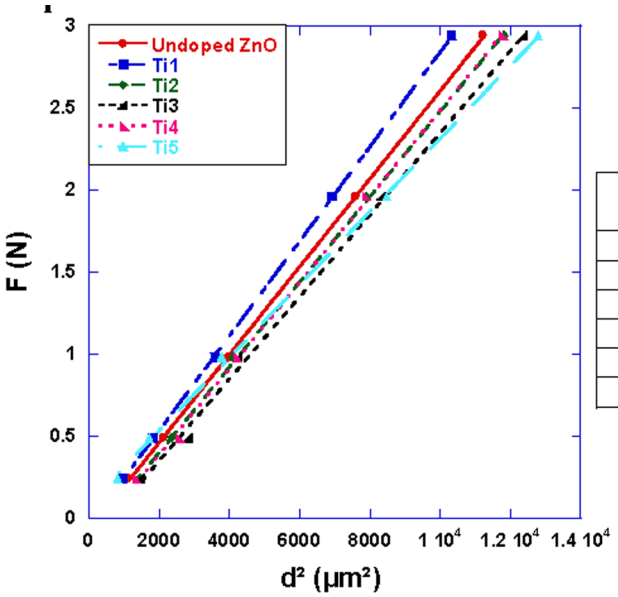


Samples	d_e (µm)	H_{EPD} (GPa)	H_v (GPa)
Undoped	-0.0684	0.523	0.458-0.486
Ti1	-0.0366	0.548	0.508-0.528
Ti2	-0.1362	0.542	0.443-0.461
Ti3	-0.1623	0.529	0.426-0.439
Ti4	-0.1420	0.548	0.434-0.463
Ti5	0.0996	0.373	0.426-0.480

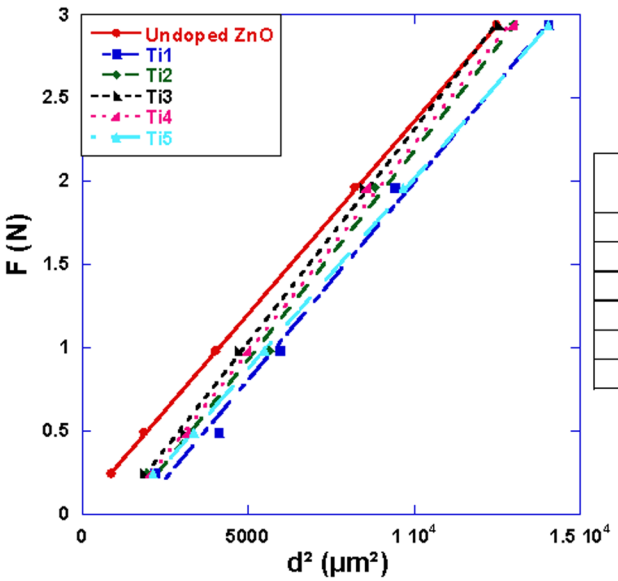


Samples	de (µm)	HEPD (GPa)	Hv (GPa)
Undoped	0.0551	0.406	0.436-0.451
Ti1	-0.3787	0.580	0.305-0.388
Ti2	-0.3176	0.587	0.321-0.419
Ti3	-0.2693	0.594	0.387-0.435
Ti4	-0.3039	0.600	0.364-0.419
Ti5	-0.2801	0.529	0.330-0.388

Fig. 6 $F^{1/2}$ -d plots of Ti doped ZnO nanoparticles synthesized with MEA and 2-Propanol solvents



Samples	$A_{HK}\times10^{-4}$ (GPa)	W_{HK} (µm)	H_{HK} (GPa)	H_v (GPa)
Undoped	2.67	-0.0672	0.495	0.458-0.486
Ti1	2.88	-0.0353	0.534	0.508-0.528
Ti2	2.59	-0.1118	0.480	0.443-0.461
Ti3	2.49	-0.1426	0.461	0.426-0.439
Ti4	2.61	-0.1296	0.484	0.434-0.463
Ti5	2.21	0.0969	0.409	0.426-0.480



Samples	$A_{HK}\times10^{-4}$ (GPa)	W_{HK} (µm)	H_{HK} (GPa)	H_v (GPa)
Undoped	2.31	0.049	0.428	0.436-0.451
Ti1	2.37	-0.377	0.439	0.305-0.388
Ti2	2.50	-0.317	0.463	0.321-0.419
Ti3	2.55	-0.243	0.472	0.387-0.435
Ti4	2.50	-0.269	0.463	0.364-0.419
Ti5	2.28	-0.262	0.422	0.330-0.388

Fig. 7 F-d_2 plots of Ti doped ZnO nanoparticles synthesized with MEA and 2-Propanol solvents

and 2-Propanol solvents are presented in tabular form. For the samples prepared using the MEA solvent, negative W_{HK} values were observed in undoped ZnO and in samples containing Ti1-Ti4, indicating that only plastic deformation occurred in these samples. In contrast, the Ti5 sample exhibited a positive W_{HK} value, signifying the presence of both elastic and plastic deformation.

In the system with 2-Propanol as the solvent, a different deformation behavior was observed. A positive W_{HK} value was obtained for the undoped ZnO sample, confirming the presence of elastic deformation. However, all Ti-doped samples showed negative W_{HK} values, indicating that plastic deformation was dominant. In both solvent systems, the microhardness values calculated using the HK model deviate from the plateau region of the load–microhardness curve, especially in samples exhibiting purely plastic deformation. This suggests that the HK model is inadequate for determining the true hardness values of materials exhibiting ISE-dominated behavior. Nevertheless, for the Ti5 samples, the HK model provided relatively more consistent results in both MEA and 2-Propanol systems. Therefore, it is considered that the HK model is only suitable for samples exhibiting dual-mode deformation (both elastic and plastic). On the other hand, for undoped ZnO and ISE-dominated samples with low Ti content, none of the models applied so far have been able to reflect the actual microhardness values near the plateau region. To overcome these limitations and more accurately analyze structures dominated by

plastic deformation, the IIC (Indentation-Induced Cracking) model, based on a crack-initiated fracture mechanism, has been considered as an alternative approach.

3.3.5 Analysis according to the indentation induced cracking (IIC) model

The IIC (Indentation-Induced Cracking) model is an approach that focuses on crack formation occurring on the material surface during microhardness tests. It is particularly used for evaluating the mechanical properties of brittle materials such as ceramics, glasses, and hard coatings. At the core of the model lies the assumption that stress accumulation caused by the applied load around the tip of the indenter leads to the initiation of cracks on the surface. This mechanism serves as a valuable tool for understanding both the stress distribution and the deformation behavior of the material.

Developed by Li and Bradt (1996), the model offers significant advantages, especially in the analysis of materials exhibiting ISE behavior [51]. At the point of maximum penetration depth, the applied load is balanced by the total resistance of the material. This resistance comprises four main components: interfacial shear, elastic deformation, plastic deformation, and crack formation.

Within the framework of the model, the microhardness value is defined as follows:

$$H_v = \lambda_1 K_1 (F/d^2) + K_2 (F^{5/3}/d^3) \tag{13}$$

Here, λ_1 is a material-related constant, while d represents the indentation size. K_1 and K_2 are constants that depend on the geometry of the indentation and the applied load, respectively. For an ideal plastic material, the microhardness is expressed as: $H_v = K_1(F/d^2)$, $\lambda_1 = 1$ and $K_2(F^{5/3}/d^3) = 0$. For perfectly brittle solids, the expression becomes: $H_v = K_2(F^{5/3}/d^3)$ and $\lambda_1 = 0$. Load-independent microhardness values can also be determined from the second term of the Eq.

$$H_v = K\left(F^{5/3}/d^3\right)^m \tag{14}$$

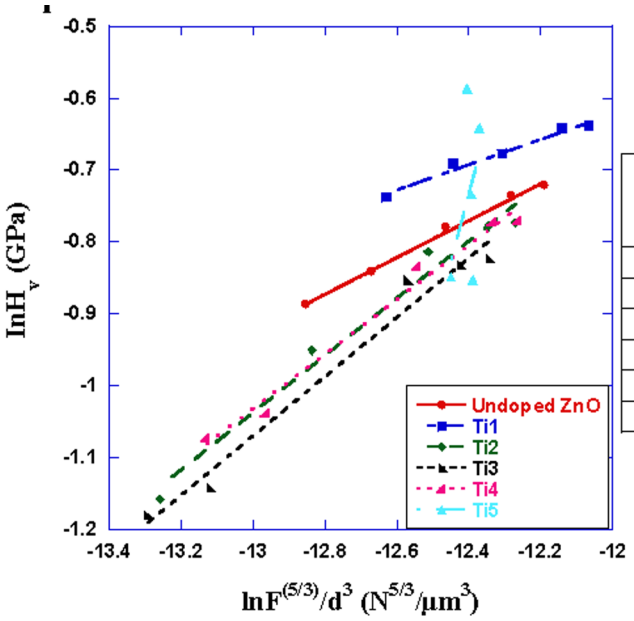
The values of *K* and *m* are load-independent constants. The exponent *m* is used to characterize the material's deformation behavior. When $m > 0.6$, the material exhibits normal ISE behavior, whereas when $m < 0.6$, it shows reverse ISE behavior [49, 52]. The values of the exponent *m*, obtained from the slope of the model's graph, are presented in Fig. 8.

In the samples prepared using MEA as the solvent, analysis of the *m* exponent values obtained from the IIC model shows that for Ti0 and Ti1-Ti4 samples, the *m* value is below 0.6. This indicates that RISE behavior is dominant in these samples. On the other hand, the *m* value for the Ti5 sample exceeds 0.6, confirming conventional ISE behavior. These results are consistent with the previous deformation analyses and support the behavior of samples exhibiting both deformation modes. Several studies in the literature [39, 53–56] have emphasized that, for the load-independent microhardness value to reflect the true microhardness, the microhardness–load curve should approach the plateau region. In this context, for the MEA-based samples, the IIC model has been clearly demonstrated to be the most appropriate approach for load-independent microhardness analysis of RISE-type materials. In contrast, for the Ti5 sample exhibiting ISE behavior, the HK model appears to be the most suitable.

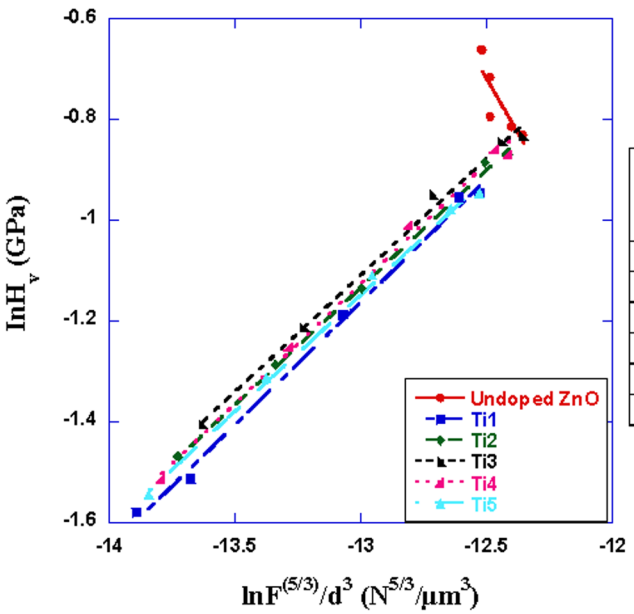
Similarly, in the analysis of samples prepared with 2-Propanol using the IIC model, the *K* and *m* constants obtained from Eq. 16 provided valuable insight for evaluating load-independent microhardness. In all Ti-doped samples, *m* values were calculated to be less than 0.6, which confirms the RISE behavior previously identified through H_v-*F* plots. Therefore, the IIC model is the most appropriate evaluation method for all RISE-characteristic samples synthesized in the 2-Propanol system. In contrast, for the undoped ZnO sample showing ISE behavior, the HK model is deemed more suitable. This comprehensive assessment reveals that in Ti-doped ZnO-based systems, identifying the appropriate microhardness model based on the deformation mechanism is critical. The IIC model stands out in the analysis of brittle structures dominated by plastic deformation and exhibiting RISE behavior, whereas the HK model remains valid for systems in which both elastic and plastic deformation are observed simultaneously.

In summary, multiple models were employed to analyze the indentation size effect (ISE) and its physical origins in the $Zn_{1-x}Ti_xO$ system. While Meyer's Law provided a basic empirical fit, it lacked a physical basis for the observed variations. The Hays-Kendall (HK) model suggested that a minimum load is required for plastic deformation, but it failed to account for the frictional effects at the indenter interface. Similarly, the Elastic-Plastic Deformation (EPD) model, which focuses on the work done during indentation, was found to be less sensitive to the specific morphological transitions—such as the densely packed flower-like structures—observed in our samples.

Furthermore, while the Indentation Induced Cracking (IIC) model is essential for toughness evaluation, its dependence on crack geometry introduces higher uncertainty in nanostructured powders compared to load-independent microhardness models. Therefore, the Proportional Sample Resistance (PSR) model is identified as the most reliable framework for this study. By effectively partitioning the



Samples	m	ln K ($N^{(3-5m)/3}/\mu m^{(2-3m)}$)	H_{HK} (GPa)
Undoped	0.25	2.40	0.486
Ti1	0.17	1.49	0.546
Ti2	0.39	4.13	0.453
Ti3	0.41	4.29	0.396
Ti4	0.37	3.89	0.457
Ti5	1.87	22.48	0.492



Samples	m	ln K ($N^{(3-5m)/3}/\mu m^{(2-3m)}$)	H_{HK} (GPa)
Undoped	0.86	-11.50	0.469
Ti1	0.48	5.16	0.290
Ti2	0.46	4.91	0.330
Ti3	0.46	4.90	0.359
Ti4	0.47	5.08	0.343
Ti5	0.46	4.85	0.316

Fig. 8 $\ln H_V$ - $F^{(5/3)}/d^3$ graphs of Ti doped ZnO nanoparticles synthesized with MEA and 2-Propanol solvents

applied load into surface energy and frictional resistance components, the PSR model provides a more robust and physically consistent interpretation of the load-independent microhardness across both MEA and 2-propanol based groups.

3.3.6 General evaluation of mechanical properties

The effects of different types of solvents on the mechanical properties of the materials were comparatively analyzed in Table 3, and the findings are summarized below in bullet points.

- The MEA solvent led to the formation of harder, stiffer, and mechanically stronger structures in the samples. This is likely due to MEA's complexation capability, which enables a more homogeneous ion distribution in the solution and results in a more compact microstructure. In contrast, the samples prepared with 2-propanol exhibited tougher structures with higher impact resistance. This can be attributed to a more porous structure, which slows down crack propagation.
- Ti-doped ZnO nanostructures synthesized using MEA exhibited higher microhardness, elastic modulus, and structural stiffness. On the other hand, nanostructures

Table 3 Mechanical test results obtained as a result of the experiments

Mechanical Property	Sample	MEA	2-Propanol	Comment
Microhardness (H_V)	Undoped	0.412–0.486	0.436–0.515	Higher hardness with MEA
	Ti doped	0.307–0.556	0.206–0.435	
Modulus of Elasticity (GPa)	Undoped	33.769–39.834	42.21–35.73	More structural rigidity with MEA
	Ti doped	25.162–45.571	16.88–35.65	
Yield Strength (GPa)	Undoped	0.137–0.162	0.171–0.145	Higher strength with MEA
	Ti doped	0.102–0.185	0.068–0.145	
Fracture Toughness ($GPa/m^{1/2}$)	Undoped	38.01–41.29	34.85–37.88	Higher toughness with 2-propanol
	Ti doped	30.79–57.59	50.13–78.14	

obtained using 2-propanol showed relatively lower microhardness and elastic modulus, yet demonstrated higher fracture toughness. Based on these findings, MEA is considered more suitable for applications requiring high mechanical strength, rigidity, and resistance to deformation. Conversely, 2-propanol offers advantages in applications where impact resistance and flexibility are essential.

- Microhardness (H_v) results indicate that ZnO and Ti-doped ZnO samples synthesized using MEA generally exhibit higher microhardness values. Although undoped ZnO samples prepared with 2-propanol showed higher microhardness under low loads (0.245 N and 0.490 N), samples synthesized with MEA outperformed them when the load increased to 0.980 N and above. This suggests that the effect of the solvent type is more pronounced at low loads, while the structural contribution of MEA becomes dominant under higher loading conditions. For Ti-doped ZnO samples, MEA consistently resulted in higher microhardness values across all load levels. For example, in the Ti1 sample, MEA-based synthesis yielded microhardness values approximately 56.9% higher under low loads. However, as the load increased, this difference decreased to about 26%. A similar trend was observed in the Ti2 sample, where the microhardness difference dropped from around 27% at low loads to 9–10% at higher loads. These findings clearly show that MEA contributes more significantly to microhardness at lower loads.
- Measurements for the Ti3 sample further confirm MEA's effectiveness in enhancing microhardness at low load levels. Under such conditions, the microhardness difference was around 20%, but this dropped to below 1% under higher loads—nearly disappearing. A similar pattern was observed for the Ti4 sample: under low loads, MEA-based samples exhibited approximately 35% higher microhardness compared to those synthesized with 2-propanol, whereas this difference dropped to around 9% at higher loads. The most pronounced difference was recorded for the Ti5 sample: under low-load applications, the MEA-based sample showed a microhardness increase of up to 61.7%, while under higher loads, the difference remained in the 9–12% range. These results suggest that MEA contributes to the formation of a more compact and rigid microstructure under low loads, and although this effect diminishes with increasing load, it does not disappear entirely. Thus, the influence of solvent type on microhardness behavior is dependent on the applied load level.
- Overall, Ti-doped ZnO samples synthesized with MEA demonstrated superior performance in terms of microhardness. Samples prepared with 2-propanol generally showed lower microhardness, particularly at lower load levels. As the load increased, the microhardness difference related to solvent type tended to diminish. However, in certain samples-particularly Ti1 and Ti5-MEA provided a significant advantage, with microhardness differences exceeding 50%. These findings highlight that solvent type is a critical parameter for enhancing the mechanical properties of ZnO-based nanostructures. While MEA is more suitable for applications requiring high rigidity, microhardness, and mechanical strength, 2-propanol may be preferred in systems where impact resistance and flexibility are prioritized.

3.4 VSM Analysis of Nanopowder Materials

In this study, the magnetic moment responses of ZnO nanopowder samples doped with transition metal Ti (IV) to an external magnetic field were determined using the Vibrating Sample Magnetometer (VSM) method. The samples were subjected to M-H (magnetization-magnetic field) measurements under a magnetic field applied in the range of ±40,000 Oe at a temperature of 300 K. Generally, for semiconductors like ZnO to exhibit ferromagnetic properties, doping with transition metals is required. In this study as well, the addition of Ti to the ZnO samples generally resulted in ferromagnetic behavior. Figure 9 shows the magnetic field curves corresponding to the magnetic moment curves. Given that Ti^{4+} ions are nominally non-magnetic, the ferromagnetic behavior is likely not an intrinsic property of the dopant ions themselves, but rather suggests a mechanism involving structural defects or solvent-induced variations. Instead, Ti doping plays a twofold role: first, due to its low solubility in the ZnO lattice, it stabilizes a large number of zinc vacancies which act as the primary source of localized magnetic moments. Second, Ti acts as a donor, increasing the concentration of charge carriers. Consequently, as Shao

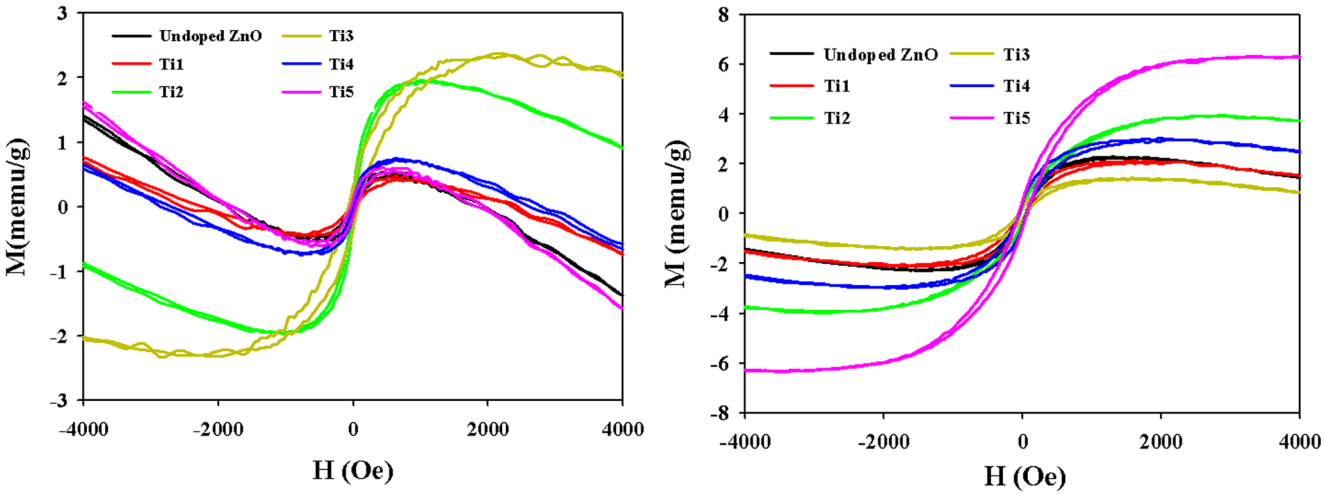


Fig. 9 Graphs of M-H for undoped and Ti doped ZnO nanoparticles synthesized using MEA and 2-Propanol solvents

et al. revealed, the observed ferromagnetism is potentially attributed to carrier-mediated exchange interactions through defect sites, such as oxygen or zinc vacancies, which are commonly discussed in doped ZnO systems.

The Ti0 samples prepared in both solvent environments exhibited low magnetic moments, as expected, and did not show any significant ferromagnetic behavior. This is consistent with the paramagnetic or diamagnetic nature of ZnO. However, the measured coercivity (H_c) values varied significantly depending on the solvent: in the MEA environment, the H_c value of undoped ZnO was 759.61 Oe, whereas in 2-propanol, it was only 40.06 Oe. This remarkable difference in coercivity can be correlated with our structural findings. XRD and SEM analyses showed that MEA produces much smaller crystallite sizes and flower-like morphology with a more densely packed structure. The higher coercivity observed in MEA-based samples may be indicative of a domain wall pinning effect, potentially influenced by the unique flower-like morphology which differs significantly from the spherical structures obtained with 2-propanol.

In both solvents, the magnetic moment increased and the hysteresis loop broadened after Ti1 doping. However, the H_c value in the MEA environment was much higher at 1198.5 Oe, while it was only 64.64 Oe in 2-propanol. This indicates that MEA facilitates stronger interactions between the dopants and the ZnO matrix, thus influencing the spin ordering more effectively. On the other hand, a higher remanent magnetization (M_r) value (0.41 memu/g) was observed in 2-propanol. At Ti2 doping, ferromagnetic properties started to become more evident in both solvents. Although the H_c value was quite low in the sample prepared with MEA (16.5 Oe), it was higher in 2-propanol at 39.48 Oe. Interestingly, the saturation magnetization (M_s) value was significantly higher in 2-propanol (3.97 memu/g) than in MEA (1.97 memu/g), which can be attributed to better Ti solubility and the formation of larger, lower-strain crystallites in 2-propanol, allowing more Ti ions to integrate into the ZnO structure (Table 4).

The emergence of ferromagnetism in the absence of magnetic ions (d^0 ferromagnetism) can be justified through the formation of donor/acceptor states associated with intrinsic defects. The substitution of Zn^{2+} by Ti^{4+} encourages the formation of oxygen vacancies (V_O) to maintain charge neutrality. Within the framework of the Bound Magnetic Polaron (BMP) model, these defects act as centers that mediate exchange interactions between localized spins, thereby inducing a macroscopic ferromagnetic response despite the non-magnetic nature of the Ti dopant. This is further supported by the clear M-H hysteresis loops observed for all doped samples, confirming that the magnetism is a defect-driven characteristic rather than an intrinsic property of the dopant ions.

At Ti3 doping, the Hc value remained low in MEA (71.91 Oe), while the M_s value was 2.35 memu/g. In 2-propanol, the H_c value was slightly higher (49.98 Oe), but the M_s value was considerably lower (1.42 memu/g). This indicates that MEA is more effective in enhancing magnetic moment at 3% Ti doping, suggesting a better magnetic structure is achieved in this solvent at that doping level. With Ti4 doping, ferromagnetic behavior became more prominent in both solvents, and the hysteresis loops widened. However, the H_c value in MEA was very high (1317.6 Oe), while it was 52.71 Oe in 2-propanol, once again confirming the strong domain wall pinning effect caused by MEA's highly stressed, fine-grained structure. Nonetheless, the M_s value in 2-propanol (3.00 memu/g) was higher than that in MEA (1.11 memu/g).

At the highest doping level of Ti5, the difference between the solvents became more pronounced. In the MEA-prepared sample, a decrease in magnetic moment was observed (M_s=2.29 memu/g), with an H_c of 937.44 Oe. In

Table 4 Magnetic parameters of samples prepared with MEA and 2-Propanol solvents

Ti (%)	H_c (Oe) MEA	M_s (memu/g) MEA	M_r (memu/g) MEA	H_c (Oe) 2-Propanol	M_s (memu/g) 2-Propanol	M_r (memu/g) 2-Propanol
0.0	759.61	2.37	0.13	40.06	2.28	0.31
1.0	1198.5	1.17	0.09	64.64	2.13	0.41
2.0	16.5	1.97	0.18	39.48	3.97	0.28
3.0	71.91	2.35	0.32	49.98	1.42	0.21
4.0	1317.6	1.11	0.08	52.71	3.0	0.46
5.0	937.44	2.29	0.12	57.71	6.34	0.54

contrast, the 2-propanol sample reached the highest magnetic moment (M_s=6.34 memu/g), and the hysteresis loop was considerably wider. This distinct divergence at 5% doping can be explained by the low solubility limit of Ti in the ZnO wurtzite structure combined with the solvent-induced microstructural differences. MEA's strong complexation leads to a highly stressed and tightly packed structure (as seen in our XRD and SEM results). At high doping levels, this compact lattice struggles to accommodate additional Ti without disrupting the spin alignment or suppressing the stabilization of further zinc vacancies, causing a drop in Ms. Conversely, 2-propanol provides a more porous, looser structure with larger crystallites and lower internal strain. This structural flexibility better accommodates the high Ti concentration near the solubility limit, keeping the carrier-mediated exchange pathways open and resulting in a record high magnetic moment.

In summary, MEA exhibits stronger coercivity (H_c) values and more pronounced hysteresis behavior at low to moderate Ti doping levels (especially at 3%), indicating stronger spin interactions and possible structural distortions in ZnO. On the other hand, 2-propanol yields higher saturation magnetization (M_s) and remanent magnetization (M_r) at higher Ti concentrations (especially at 5%), making it a more efficient solvent for applications requiring high magnetic moment. Consequently, MEA appears more suitable for applications that require high coercivity (e.g., spintronic devices) due to its fine-grained, high-strain morphology, while 2-propanol is more advantageous for applications requiring high magnetization (e.g., magnetic storage) thanks to its larger crystallites and porous lattice structure that favors higher Ti accommodation.

The correlation between structural parameters and magnetic response reveals that the choice of solvent modulates the domain wall pinning landscape. The smaller grains and higher strain in MEA-treated samples provide numerous pinning sites that enhance coercivity (H_c), whereas the larger, more relaxed crystallites in the 2-propanol group favor higher saturation magnetization (M_s) by reducing grain boundary interruptions in the ferromagnetic coupling.

In addition, to rule out the influence of extrinsic factors on the observed magnetic behavior, it should be noted that no secondary phases or metallic clusters were detected via XRD analysis. Since both Ti and its common oxide forms are inherently non-magnetic (d^0 systems), any potential sub-microscopic clustering would not account for the reported ferromagnetic response. Furthermore, the systematic and reproducible variations in saturation magnetization (M_s) and coercivity (H_c) between the MEA-based and 2-propanol-based groups indicate that the magnetism is directly coupled to the intrinsic defect states and surface-to-volume ratios unique to each synthesis route. Therefore, the possibility of transition metal contamination (e.g., Fe, Co, Ni) is minimized, and the magnetic properties can be confidently attributed to intrinsic defect-mediated exchange interactions.

The magnetic characteristics of our Ti-doped ZnO nanostructures were compared with recent literature, such as Cu/Ga-doped ZnO systems [5]. While Cu/Ga doping often enhances magnetic properties through direct s-d or p-d exchange interactions, the ferromagnetic response in our Ti-doped system is primarily driven by d^0 ferromagnetism mediated by oxygen vacancies. Specifically, the M_s and H_c values obtained in this study are consistent with those reported for sol-gel synthesized ZnO nanoparticles, yet our results highlight a unique solvent-dependent tuning of these parameters. This comparison suggests that while the dopant type dictates the electronic origin of magnetism, the synthesis medium (MEA vs. 2-propanol) remains a critical factor in optimizing the macroscopic magnetic response through morphological and defect engineering.

4 Conclusions

In this study, Ti-doped ZnO nanoparticles were successfully synthesized via the sol–gel method using MEA and 2-propanol as solvents, and the structural and mechanical properties of the resulting samples were comprehensively compared. The findings revealed that both the type of solvent and the Ti doping ratio directly influence the performance of ZnO-based nanostructures.

- XRD analyses confirmed that the hexagonal wurtzite structure of ZnO was preserved in the samples prepared with both solvents. The substitution of Zn^{2+} ions by Ti^{4+}

ions led to lattice contraction and internal stress within the crystal structure. Smaller crystallite sizes and higher internal stress were observed in the MEA-based samples, whereas 2-propanol resulted in larger crystallites and lower internal stress levels.

- SEM images showed that the samples synthesized with MEA exhibited a more compact and homogeneous morphology. In contrast, samples prepared with 2-propanol demonstrated porous, rod-like, and flower-like structures at lower doping levels. As the Ti content increased, these structures became denser and more compact.
- Mechanical tests revealed that samples synthesized with MEA exhibited higher microhardness, elastic modulus, and yield strength across all load levels, whereas those prepared with 2-propanol demonstrated significantly higher fracture toughness. The microhardness difference was particularly notable under low loads-reaching up to 60% in the Ti5 sample-but decreased as the load increased.
- ISE/RISE behavior analyses showed that conventional ISE behavior in undoped ZnO and Ti5 samples was best represented by the Hays–Kendall model, while RISE behavior in the other Ti-doped samples was more accurately described using the IIC model. The PSR and EPD models, on the other hand, showed limited success in determining load-independent microhardness values.
- All these findings indicate that both solvent selection and doping concentration play a critical role in defining the microstructure and mechanical behavior of ZnO-based nanostructures. MEA is more suitable for applications requiring high microhardness, stiffness, and mechanical strength, whereas 2-propanol is preferable in systems where impact resistance and flexibility are prioritized. This study provides significant contributions to the design and optimization of ZnO-based nanomaterials for use in applications such as sensor technologies, coatings, and optoelectronic devices.
- Magnetic (VSM) analyses revealed that Ti doping successfully induces room-temperature ferromagnetism in ZnO nanoparticles. Since Ti^{4+} ions theoretically possess zero magnetic moment, this ferromagnetic behavior originates from carrier-mediated exchange interactions between zinc vacancies stabilized by the Ti incorporation. The results clearly demonstrated that solvent-induced structural differences magnetic performance: MEA produced a highly strained, fine-grained, and compact structure that enhanced domain wall pinning, resulting in significantly higher coercivity (Hc), which is highly desirable for spintronic devices. Conversely, 2-propanol yielded a looser, more porous lattice with larger crystallites. This structural flexibility better accommodated high Ti concentrations (e.g., 5%) near the solubility limit, keeping exchange pathways intact and achieving much higher saturation magnetization (Ms), making it more advantageous for magnetic storage applications.
- The observed room-temperature ferromagnetism, coupled with the ability to tune magnetic parameters through solvent selection, highlights the potential of Ti-doped ZnO nanostructures for spintronic applications. Specifically, the transition from spherical to flower-like morphologies allows for the modulation of coercivity, which is essential for spin-polarized transport and information storage. While further studies on spin-injection efficiency are required, the current results demonstrate a feasible chemical route for developing d^0 ferromagnetic semiconductors that operate at room temperature, making them promising candidates for next-generation spin-based electronic devices.

Acknowledgements This research was funded by The Scientific and Technological Research Council of Turkey (TUBITAK), grant number 2210-C (Domestic Priority Areas Graduate Scholarship Program).

Author contributions Conceptualization, E.A.T.; methodology, H.A. and Ö.Ö.; validation, Ö.Ö. and S.S.; formal analysis, H.A. and E.T.; investigation, E.T. and H.A.; writing—original draft preparation, E.A.T.; writing—review and editing, E.A.T., S.S. and Ö.Ö.; supervision, S.S. All authors have read and agreed to the published version of the manuscript.

Funding Open access funding provided by the Scientific and Technological Research Council of Türkiye (TÜBİTAK). This research was funded by The Scientific and Technological Research Council of Turkey (TUBITAK), grant number 2210-C (Domestic Priority Areas Graduate Scholarship Program).

Data availability No datasets were generated or analysed during the current study.

Declarations

Institutional review board Not applicable.

Informed consent Not applicable.

Conflict of interest The authors declare no conflicts of interest. The funders had no role in the design of the study; in the collection, analyses, or interpretation of data; in the writing of the manuscript; or in the decision to publish the results.

Competing interests The authors declare no competing interests.

Open Access This article is licensed under a Creative Commons Attribution 4.0 International License, which permits use, sharing, adaptation, distribution and reproduction in any medium or format, as long as you give appropriate credit to the original author(s) and the source, provide a link to the Creative Commons licence, and indicate if changes were made. The images or other third party material in this article are included in the article's Creative Commons licence, unless indicated otherwise in a credit line to the material. If material is not

included in the article's Creative Commons licence and your intended use is not permitted by statutory regulation or exceeds the permitted use, you will need to obtain permission directly from the copyright holder. To view a copy of this licence, visit http://creativecommons.org/licenses/by/4.0/.

References

1. U. Özgür, D. Hofstetter, H. Morkoç, ZnO devices and applications: a review. Proc. IEEE **98**, 1255–1268 (2010)
2. T. Dietl, H. Ohno, F. Matsukura, J. Cibert, D. Ferrand, Zener model description of ferromagnetism in zinc-blende magnetic semiconductors. Science **287**, 1019–1022 (2000)
3. S.J. Pearton, D.P. Norton, M.P. Ivill, A.F. Hebard, J.M. Zavada, W.M. Chen, I.A. Buyanova, Ferromagnetism in transition-metal doped ZnO. J. Electron. Mater. **36**, 462–471 (2007)
4. S.A. Wolf, D.D. Awschalom, R.A. Buhrman, J.M. Daughton, S. VonMolnár, M.L. Roukes, A.Y. Chtchelkanova, D.M. Treger, Spintronics: a spin-based electronics vision for the future. Science **294**, 1488–1495 (2001)
5. K. Omri, Cu/Ga doped ZnO nanoparticles with improved optoelectronic and magnetic characteristics produced using the sol–gel technique. J. Sol-Gel Sci. Technol. **117**, 32 (2026)
6. K. Omri, Effect of thermal treatment on ZnO nanostructures' electrical and ferromagnetic properties. J. Aust. Ceram. Soc. **62**, 627–638 (2026)
7. H. Alali, K. Omri, S. Ansari et al., Fabrication and impact on photocatalytic activity of Cu-doped ZnO/SnO_2 nanostructures with for enhancing the electrochemical performance. Transit. Met. Chem. **50**, 323–333 (2025)
8. G. Lawes, A.S. Risbud, A.P. Ramirez, R. Seshadri, Absence of Ferromagnetism in Co and Mn Substituted Polycrystalline ZnO. Phys. Rev. B **71**, 045201 (2005)
9. G. Demircan, E.F. Gurses, B. Aktas, Ş Yalcin, A. Acikgoz, G. Ceyhan, M.V. Balak, Sol–gel synthesis of Si-ZnO, Ti-ZnO and Si-Ti-ZnO thin films: impact of Si and Ti content on structural and optical properties. J. Sol-Gel Sci. Technol. **34**, 105234 (2023)
10. M. Rajasekaran, A. Arunachalam, P. Kumaresan, Structural, morphological and optical characterizatin of Ti-doped ZnO nanorod thin film synthesized by spray pyrolysis technique. Mater. Res. Express **7**, 036412 (2020)
11. R.S. Sonawane, S.G. Hegde, M.K. Dongare, Preparation of titanium (IV) oxide thin film photocatalyst by sol–gel dip coating. Mater. Chem. Phys. **77**, 744–750 (2002)
12. C. Su, B.Y. Hong, C.M. Tseng, Sol–gel Preparation and Photocatalysis of Titanium Dioxide. Catal. Today. **96**, 119–126 (2004)
13. S.P.G. Soniya, S. Kaleemulla, Properties of Ti doped ZnO nanoparticles under solid state reaction method involving vacuum annealing. Physica B Condens. Matter **649**, 414409 (2023)
14. F. Matsukura, H. Ohno, T. Dietl, III–V Ferromagnetic Semiconductors, in *Handbook of Magnetic Materials*, vol. 1, ed. by K.H.J. Buschow (Elsevier, Amsterdam, The Netherlands, 2002), pp.1-[object Object]
15. S.J. Pearton, W.H. Heo, M. Ivill, D.P. Norton, T. Steiner, Dilute Magnetic Semiconducting Oxides. Semicond. Sci. Technol. **19**, R59–R74 (2004)
16. T. Dietl, Origin of Ferromagnetic Response in Diluted Magnetic Semiconductors and Oxides. J. Phys. : Condens. Matter. **19**, 165204 (2007)
17. J.H. Park, M.G. Kim, H.M. Jang, S. Ryu, Y.M. Kim, Ferromagnetic properties of Zn1-xMn_xO thin films. Appl. Phys. Lett. **84**, 1338–1340 (2004)
18. D.P. Norton, M.E. Overberg, S.J. Pearton, K. Pruessner, J.D. Budai, L.A. Boatner, M.F. Chisholm, J.S. Lee, Z.G. Khim, Y.D. Park, R.G. Wilson, Ferromagnetism in Cobalt-Implanted ZnO. Appl. Phys. Lett. **83**, 5488–5490 (2003)
19. P. Sati, R. Hayn, R. Kuzian, S. Regnier, S. Schäfer, A. Stepanov, C. Morhain, C. Deparis, M. Laugt, M. Goiran, Z. Golacki, Magnetic Anisotropy and Spin Polarization in $Zn_{1-x}Co_xO$ Thin Films. Phys. Rev. Lett. **96**, 017203 (2006)
20. M. Naeem, S.K. Hasanain, M. Kobayashi, Y. Ishida, A. Fujimori, S. Buzby, S.I. Shah, Magnetic Properties of Fe-Doped ZnO Nanoparticles. Nanotechnology. **17**, 2675–2680 (2006)
21. J. Hays, K.M. Reddy, N.Y. Graces, M.H. Engelhard, V. Shutthanandan, M. Luo, C. Xu, N.C. Giles, C. Wang, S. Thevuthasan, A. Punnoose, High-Temperature Ferromagnetism in Gd-Doped ZnO. J. Phys. : Condens. Matter. **19**, 266203 (2007)
22. C.B. Fitzgerald, M. Venkatesan, J.G. Lunney, L.S. Dorneles, J.M. Coey, D. Ferromagnetism in Ga-Doped ZnO. Appl. Surf. Sci. **247**, 493–496 (2005)
23. A.S. Risbud, N.A. Spaldin, Z.Q. Chen, S. Stemmer, R. Seshadri, Absence of ferromagnetism in Co- and Mn-doped ZnO. Phys. Rev. B **68**, 205202 (2003)
24. Y. Imai, A. Watanabe, Comparison of electronic structures of doped ZnO by various impurity elements calculated by a first-principle pseudopotential method. J. Mater. Sci. Mater. Electron. **15**, 743–749 (2004)
25. J. Antony, S. Pendyala, D.E. McCready, M.H. Engelhard, D. Meyer, A. Sharma, Y. Qiang, Ferromagnetism in Ti-doped ZnO nanoclusters above room temperature. IEEE Trans. Magn. **42**, 2697–2699 (2006)
26. K. Osuch, E.B. Lombardi, W. Gebicki, First principles study of ferromagnetism in Ti0.0625Zn0.9375O. Phys. Rev. B **73**, 075202 (2006)
27. T. Akilan, N. Srinivasan, R. Saravanan, Magnetic and optical properties of Ti doped ZnO prepared by solid state reaction method. Mater. Sci. Semicond. Process. **30**, 381–387 (2015)
28. N.H. Jadhav, D.R. Shinde, S.S. Sakate, N.K. Rasal, R.A. Pawar, Ti(IV) doping: an effective strategy to boost Lewis acidic performance of ZnO catalyst in fluorescein dye synthesis. Catal. Commun. **119**, 120–125 (2018)
29. M. Cingi, H. Çimenoğlu, Ti6Al7Nb alaşımının yorulma davranışı. İTÜ Dergisi/d Mühendislik **9**, 163–167 (2011)
30. E.J. Luna-Arredondo, A. Maldonado, R. Asomoza, D.R. Acosta, M.A. Meléndez-Lira, M. Olvera, Structural properties of ZnO:Al thin films obtained by chemical spray. Thin Solid Films **490**, 132–136 (2005)
31. P.T. Phong, P.H. Nam, N.X. Phuc, B.T. Huy, L.T. Lu, D.H. Manh, I.-J. Lee, Optical and electrical properties of ZnO thin films synthesized via sol–gel method. Metall. Mater. Trans. A **50**, 1571–1581 (2019)
32. R. Chauhan, A. Kumar, R.P. Chaudhary, S.K. Tripathi, K. Dharamvir, R. Kumar, G.S.S. Saini, Synthesis and optical properties of nickel doped zinc oxide nanoparticles. *AIP Conf. Proc.* 2011, *1391*
33. E. Asikuzun, O. Ozturk, Comparison of theoretical and experimental microhardness of tetrahedral binary Zn1-xEr_xO semiconductor polycrystalline nanoparticles. Ceram. Int. **45**, 4176–4183 (2019)
34. E. Asikuzun, O. Ozturk, Theoretical and experimental approaches to measuring mechanical properties of $Zn_{1-x}Co_xO$ binary tetrahedral bulk semiconductors. J. Mater. Sci. Mater. Electron. **29**, 7971–7978 (2018)
35. E. Asikuzun, O. Ozturk, H.A. Cetinkara, G. Yildirim, A. Varilci, M. Yılmazlar, C. Terzioglu, Vickers hardness measurements and some physical properties of Pr2O3 doped Bi-2212 superconductors. J. Mater. Sci. Mater. Electron. **23**, 1001–1010 (2012)
36. H. Aydın, O. Cakiroglu, M. Nursoy, C. Terzioglu, Mechanical and superconducting properties of the

Bi1.8Pb0.35Sr1.9Ca2.1Cu3Gd_xO_γ system. Chin. J. Phys. **47**, 192–206 (2009)
37. S.M. Khalil, Enhancement of superconducting and mechanical properties in BSCCO with Pb additions. J. Phys. Chem. Solids **62**, 457–466 (2001)
38. O. Ozturk, E. Asikuzun, S. Kaya, M. Erdem, S. Safran, A. Kilic, C. Terzioglu, AC susceptibility measurements and mechanical performance of bulk MgB2. J. Supercond. Nov. Magn. **28**, 1943–1952 (2015)
39. J.B. Quinn, G.D. Quinn, Indentation brittleness of ceramics: a fresh approach. J. Mater. Sci. **32**, 4331–4346 (1997)
40. L. Arda, O. Ozturk, E. Asikuzun, S. Ataoglu, Structural and mechanical properties of transition metals doped ZnMgO nanoparticles. Powder Technol. **235**, 479–484 (2013)
41. U. Kölemen, O. Uzun, M. Yılmazlar, N. Güçlü, E. Yanmaz, Hardness and microstructural analysis of Bi1.6Pb0.4Sr2Ca2-xSm_xCu3O polycrystalline superconductors. J. Alloys Compd. **415**, 300–306 (2006)
42. O. Sahin, O. Uzun, M. Sopicka-Lizer, H. Gocmez, U. Kölemen, Dynamic hardness and elastic modulus calculation of porous SiAlON ceramics using depth-sensing indentation technique. J. Eur. Ceram. Soc. **28**, 1235–1242 (2008)
43. H. Koralay, O. Hicyilmaz, S. Cavdar, E. Asikuzun, A.T. Tasci, O. Ozturk, Effect of Zn content on microstructure and mechanical performance in Bi1.8Sr2Ca2Cu3.2-xZn_xO10+δ glass ceramic. J. Mater. Sci.: Mater. Electron. **25**, 3116–3126 (2014)
44. E. Meyer, VDI Z. **52**, 645 (1908)
45. O. Ozturk, H.A. Cetinkara, E. Asikuzun, M. Akdogan, M. Yilmazlar, C. Terzioglu, Investigation of mechanical and superconducting properties of iron diffusion-doped Bi-2223 superconductors. J. Mater. Sci. : Mater. Electron. **22**, 1501–1508 (2011)
46. B.W. Mott, *Microindentation Hardness Testing* (Butterworths, London, UK, 1956)
47. M.L. Tarkanian, J.P. Neumann, L. Raymond, *The Science of Hardness Testing and Its Research Applications*; ASME: Metal Park, OH, USA, 1973
48. G.P. Upit, S.A. Varchenya, Microhardness of alkali halide crystals. Phys. Status Solidi B **17**, 831–835 (1966)
49. S.J. Bull, T.F. Page, E.H. Yoffe, An explanation of the indentation size effect in ceramics. Philos. Mag. Lett. **59**, 281–287 (1989)
50. C. Hays, E.G. Kendall, An analysis of Knoop microhardness. Metallography. **6**, 275–282 (1973)
51. H. Li, R.C. Bradt, The effect of indentation-induced cracking on the apparent microhardness. J. Mater. Sci. **31**, 1065–1070 (1996)
52. K. Sangwal, On the reverse indentation size effect and microhardness measurement of solids. Mater. Chem. Phys. **63**, 145–152 (2000)
53. J. Gong, J. Wu, Z. Guan, Examination of the indentation size effect in low-load Vickers hardness testing of ceramics. J. Eur. Ceram. Soc. **19**, 2625–2631 (1999)
54. Z. Peng, J. Gong, H. Miao, On the description of indentation size effect in hardness testing for ceramics: analysis of the nanoindentation data. J. Eur. Ceram. Soc. **24**, 2193–2201 (2004)
55. H. Li, Y. Huang, Q. Zhang, Y. Qiao, G. Yousong, J. Liu, Y. Zhang, ZnO-based materials for photocatalytic and antibacterial applications. RSC Adv. **3**, 654–660 (2011)
56. Q. Shao, C. Wang, J.A. Zapien, C.W. Leung, A. Ruotolo, Ferromagnetism in Ti-doped ZnO thin films. J. Appl. Phys. **117**, 17B908 (2015)

Publisher's Note Springer Nature remains neutral with regard to jurisdictional claims in published maps and institutional affiliations.